2

Land surface–atmosphere parameterizations

2.1 Introduction

It is always enjoyable to walk outside on a cool, clear, crisp day and feel the sun warming your clothes and skin, taking the chill away. The sun's radiation also plays a similar role for the Earth's surface. As sunlight reaches the surface, some of it is reflected back to space, but much of it is absorbed and acts to warm the Earth's surface. In addition, the atmosphere emits longwave (infrared) radiation that acts to warm the surface. The energy provided by these two radiation sources must either be stored in the ground or transferred to the atmosphere via sensible and latent heat flux and longwave radiative flux. The partitioning of this energy into the storage and sensible and latent heat components plays a large role in determining the temperature and humidity near the ground surface, making a day strolling in the park either pleasant or uncomfortable.

The variation in the sensible and latent heat fluxes from location to location is significant (Fig. 2.1). Some of the variations in total flux are due to location influencing the amount of radiation reaching the ground surface. However, much of the horizontal variation in the relative amounts of sensible and latent heat flux is due to the ground surface conditions. The soil type, vegetation type and health, and soil moisture all strongly influence how much energy is partitioned into sensible heat flux (warming) and how much energy is partitioned into latent heat flux (moistening). One can take the same location on the same day and artificially alter the ground conditions in a model such that the curves of sensible and latent heat flux are reversed from what is seen in Fig. 2.1, further illustrating the wide variety of responses that can occur due to surface conditions. This partitioning of sensible and latent heating has a huge influence on the near-surface variables, the depth and structure of the boundary layer, and the potential for precipitation.

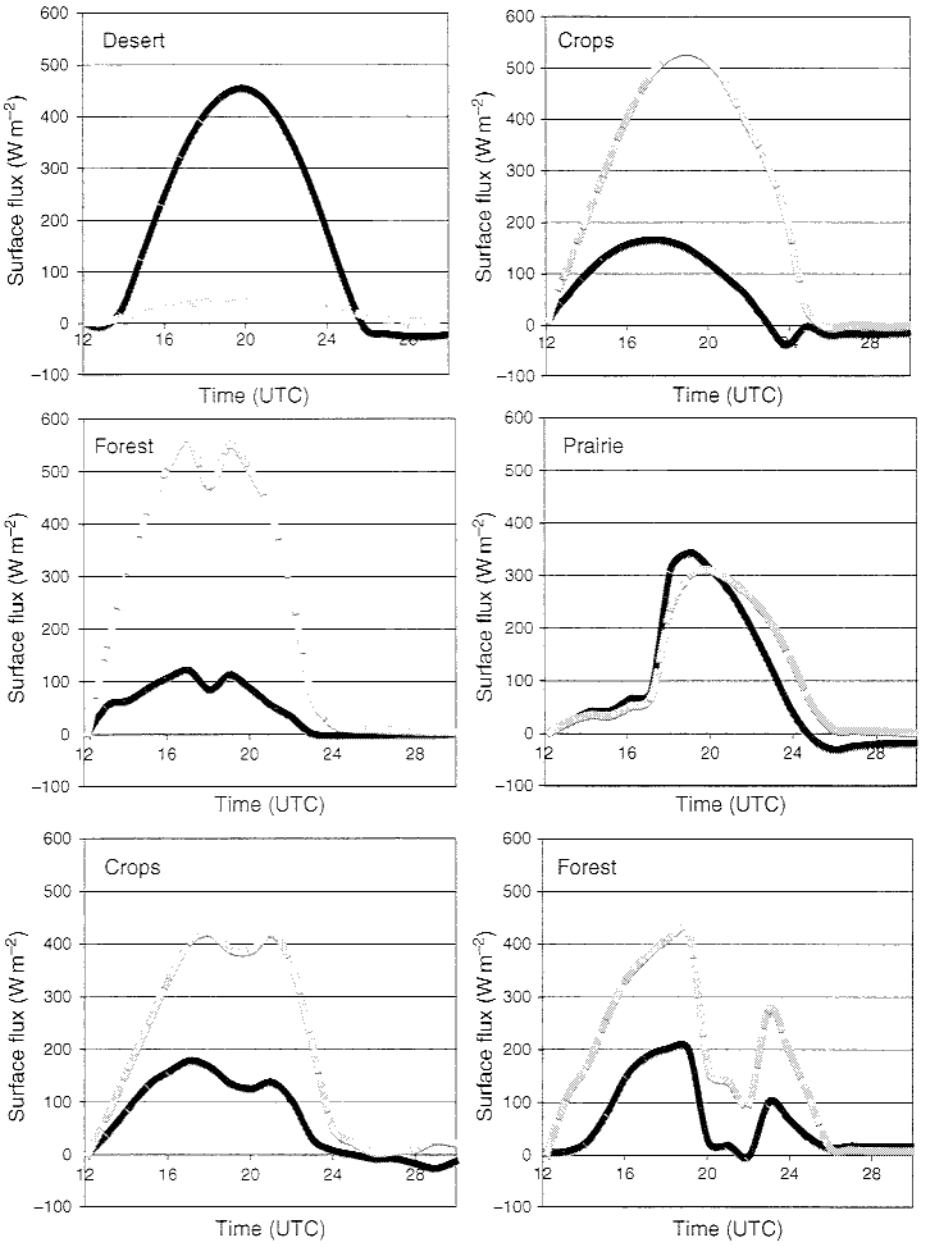

Figure 2.1. Numerical model predictions of sensible (black) and latent (gray) heat fluxes versus time (UTC in hours) for different locations over North America. The general vegetation present at the ground surface is indicated. Note that maximum of the sum of the sensible and latent heat flux is roughly 600 W m^{-2} in many of the curves, yet the partitioning between the sensible and latent heat fluxes is quite different. Thus, the underlying ground surface and vegetation are important to predicting the near-surface variables in NWP models.

If variations in surface conditions occur over small scales, then the resulting rapid horizontal changes in the values of the surface fluxes can lead to the development of non-classical mesoscale circulations, such as vegetation or inland sea breezes (Anthes 1984; Ookouchi *et al.* 1984; Mahfouf *et al.* 1987; Segal and Arritt 1992; Segal *et al.* 1988; Smith *et al.* 1994; Segele *et al.* 2005). Variations in surface fluxes owing to the harvesting of winter wheat or irrigation, leading to gradients in the surface fluxes over a mesocale-sized region, are observed to lead to dramatic differences in surface temperatures and even low-level cloud formation (Segal *et al.* 1989; Rabin *et al.* 1990; McPherson *et al.* 2004). Differential heating due to changes in surface conditions also can play important roles in enhancing baroclinic zones associated with frontal boundaries (Chang and Wetzel 1991), drylines (Benjamin and Carlson 1986; Lakhtakia and Warner 1987; Lanicci *et al.* 1987), the development of the low-level jet (McCorcle 1988) and the capping inversion (Lanicci *et al.* 1987; Beljaars *et al.* 1996), and the development and evolution of precipitation systems (Lakhtakia and Warner 1987; Lanicci *et al.* 1987; Segal *et al.* 1989; Beljaars *et al.* 1996).

On longer timescales, numerical simulations indicate that surface conditions and their heterogeneity are important to seasonal forecasting (Oglesby and Erickson 1989; Pielke *et al.* 1991; Arpe *et al.* 1998; Koster and Suarez 2001; Ronda *et al.* 2002; Douville 2003; Gedney and Cox 2003; Zhang and Fredriksen 2003). Often the effect of surface conditions, such as soil moisture, influences regions far removed from the soil moisture anomalies owing to the effects of advection. However, at other times the local fluxes can be important to precipitation, as suggested for the 1993 midwestern United States flood event (Trenberth and Guillemot 1996), or to the maintenance of drought conditions (Oglesby and Erickson 1989; Trenberth and Guillemot 1996). One conclusion from all these studies is that surface conditions, such as soil moisture and its local variation, can have a long memory and influence both short-term and seasonal features in the atmosphere.

Owing to these studies and others, it was realized in the early 1980s both that the land surface plays a substantial and important role in what happens in the atmosphere on all scales and that our abilities to model this important component of the land–atmosphere system were limited. Therefore, the exploration of numerical model parameterizations begins at the Earth's surface and the terms in the surface energy budget that govern how conditions change near the ground are surveyed.

2.2 Overview of the surface energy budget

The surface energy budget that defines the energy balance at the infinitesimally thin Earth–atmosphere boundary is composed of four main terms: net radiation, sensible heat flux, latent heat flux, and ground heat flux. The net radiation

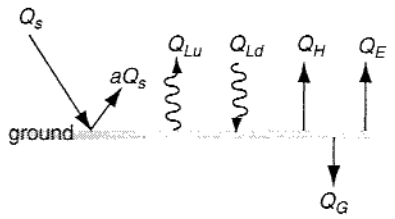

Figure 2.2. Schematic of the fluxes associated with the surface energy budget during a typical daytime situation when incoming solar radiation is present. The arrows indicate the direction of flux relative to the ground surface. Terms are defined in the text.

term typically is separated into parts representing the incoming shortwave radiation from the sun, the reflected shortwave radiation, longwave downwelling radiation, and longwave upwelling radiation. These terms can be sketched on a surface energy budget diagram as in Fig. 2.2, where the direction of the arrow designates the direction of energy transfer.

In the figure, Q_S is the incoming solar radiation, aQ_S is the reflected solar radiation (where a is the albedo), Q_{Lu} is the upwelling longwave radiation from the surface, Q_{Ld} is the downwelling longwave radiation from the atmosphere, Q_H is the sensible heat flux, Q_E is the latent heat flux, and Q_G is the ground heat flux. Unfortunately, the sign conventions for the flux values are inconsistent in the literature. The plus sign is sometimes used to mean that the fluxes are upward into the atmosphere, but sometimes the minus sign is used. The best way to approach this problem is to pay attention to the direction of the flux arrows, i.e. determine if the flux is acting to warm or cool the surface, and then apply the sign that is needed. The surface energy budget simply specifies that the amount of energy going into the surface equals the amount of energy leaving the surface. There is no storage of energy since the Earth–atmosphere boundary is assumed to have zero thickness and no mass.

What processes affect these surface energy budget terms, and thus need to be included in any numerical weather prediction model? Let us take a look term by term.

2.2.1 Incoming solar radiation (Q_S)

The incoming solar radiation that reaches the Earth's surface depends upon a number of factors. The first factor is the amount of radiant energy from the sun that reaches the top of the atmosphere. This amount is related to the solar constant, the amount of radiant energy flux per unit area passing through a plane normal to the solar beam at the Earth's mean distance from the sun. Thus, the radiant energy

from the sun that reaches the top of the atmosphere varies with the distance from the sun, and since the Earth's orbit is an ellipse, it varies throughout the year. In some models, the amount of radiant energy at the top of the atmosphere represents the yearly average value. Other models allow the solar radiant energy at the top of the atmosphere to vary by including the effect of the elliptical orbit.

Measurements of the solar constant from space also indicate variability on timescales much longer than the orbital period (Fig. 2.3). Sunspot activity appears to influence the solar constant. In addition, different instruments provide different values for the constant. It appears that there is still more to learn about the solar constant, although some value must be used. Typical values range from 1365 to 1374 W m^{-2}, with the generally accepted value being 1368 W m^{-2}.

Incoming solar radiation may be viewed as a continuous electromagnetic spectrum of waves with wavelengths of approximately 0.15–4.0 μm and with a maximum emission near 0.475 μm corresponding to blue light. Approximately 40% of this spectrum lies in wavelengths within the visible region of 0.4–0.7 μm, 50% in wavelengths longer than visible (infrared), and 10% in wavelengths shorter than visible (ultraviolet). The solar radiation that reaches the Earth's surface is influenced by the path length – the total distance through the atmosphere that the radiant energy passes. When the sun is directly overhead, the path

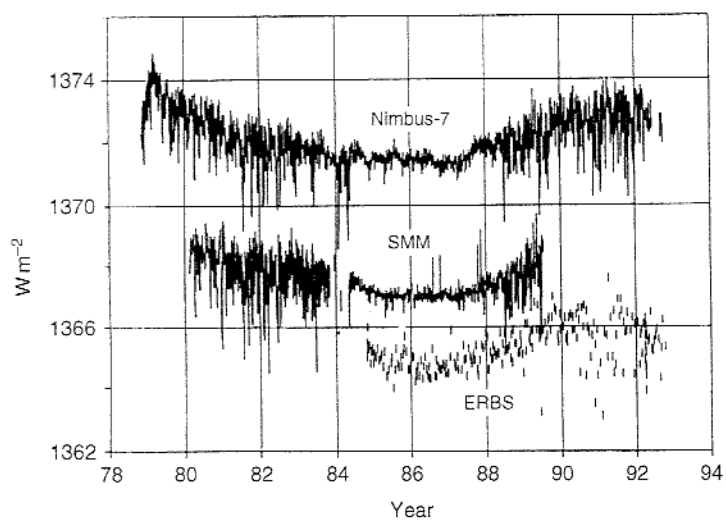

Figure 2.3. Measurements of the solar constant over a more than ten-year period from three different satellites in orbit around the Earth. Note both the longer period cycles, that correspond to sunspot activity, and the different average values produced from the three sensors. The solar constant is difficult to measure accurately, owing to uncertainties in the absolute calibrations, leading to uncertainty in its actual value. From Foukal (1994).

length is defined to be 1. As the sun moves toward the horizon, the path length increases. This is important to the intensity of incoming solar radiation at the surface because as the path length increases more of the radiant energy is scattered by molecules in the atmosphere. In addition, the angle between the Earth's surface and the beam of incoming solar radiation, called the angle of incidence, directly affects the intensity of the radiation that reaches the surface. Just as longer shadows occur early and late in the day, the incoming solar radiation is spread over a larger area when the beam of light from the sun is not perpendicular to the surface, thereby decreasing its intensity over a fixed area.

Cloudiness has a large influence on solar radiation. Cloud droplets act to both scatter and absorb solar radiation. When a photon enters a cloud, it is scattered back and forth by particles of water or ice until it either escapes or is absorbed. Clouds typically appear white because all the colors within sunlight scatter out of the cloud equally. Individually, small clouds may not have a huge influence on the amount of solar radiation that reaches the surface, although the combined effects of many small clouds can be considerable. However, when light enters a large storm cloud, very little of it passes through to the ground. In these situations, blue or green colors can sometimes be seen as one looks up into the cloud. Particles from pollution and aerosols also influence the incoming solar radiation in ways very similar to those of clouds.

Clouds arguably represent the greatest uncertainty in climate change simulations that examine the potential consequences to continued global increases in greenhouse gases owing to the burning of fossil fuels. In addition to both absorbing and scattering solar radiation, clouds absorb and emit longwave radiation, making them very important contributors to the radiation balance of the atmosphere.

Finally, the slope of the ground surface changes the angle of incidence. In regions of steep terrain, some slopes may not receive any direct solar radiation, while in other areas the slopes may receive direct radiation only starting several hours after sunrise (Fig. 2.4). Other parts of the steep terrain may be oriented nearly perpendicular to the direct beam of the solar radiation during certain parts of the year, and thereby receive more solar radiation than expected from a flat surface at these times. Thus, gradients in the incoming solar radiation can be quite large when the terrain is complex, and can feed back and influence the vegetation that survives (Fig. 2.5).

2.2.2 Albedo (a)

Albedo is the fraction (0 to 1) of the incoming solar radiation that is reflected upward from the Earth's surface. For bare surfaces, the albedo is influenced by the soil type. Sand reflects more solar radiation than black dirt, which explains

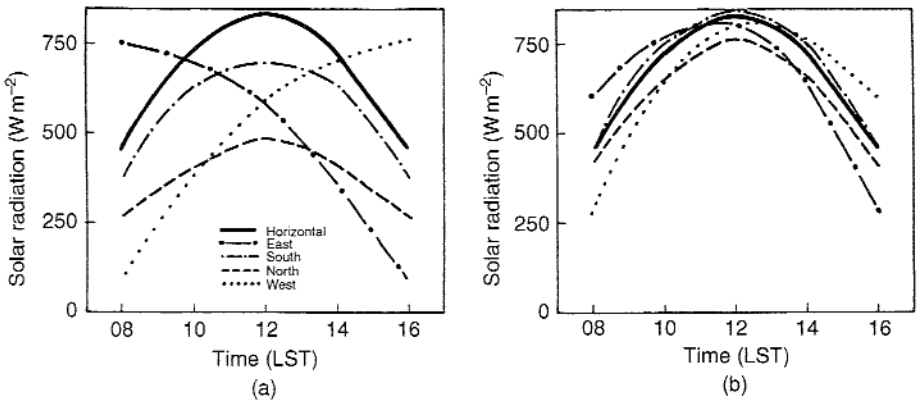

Figure 2.4. Diurnal variation of solar global radiation received on a horizontal surface and on uniformly sloping terrain facing north, south, east, and west on 15 July at a latitude of 37° N. Uniform slope inclinations are (a) 45° and (b) 15°. From Avissar and Pielke (1989).

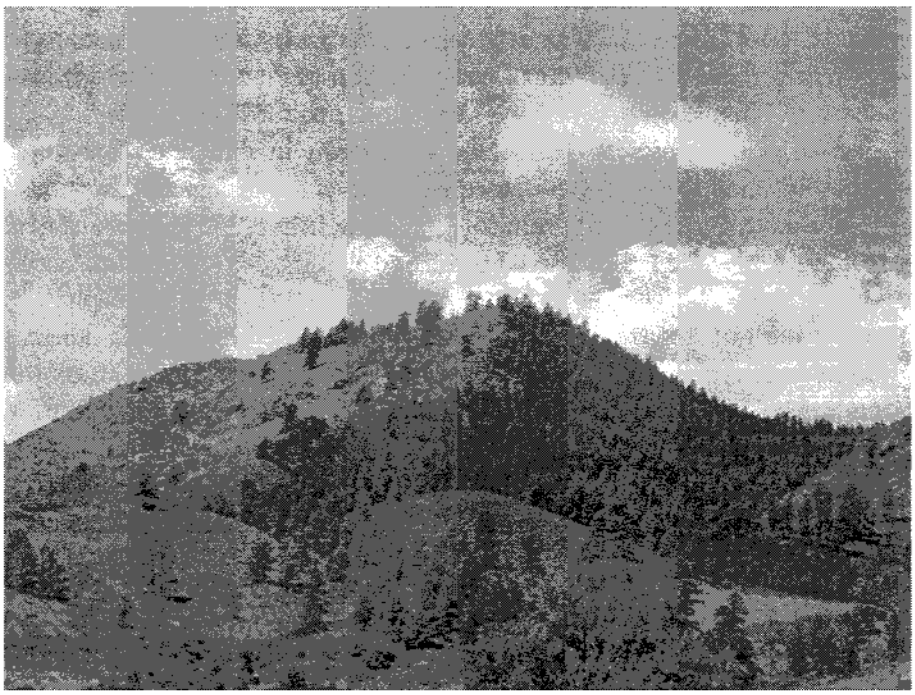

Figure 2.5. A mountain ridge near Fort Collins, Colorado, illustrating the vegetation contrast on a south-facing slope (left side of ridge) and a north-facing slope (right side of ridge). Also see Avissar and Pielke (1989).

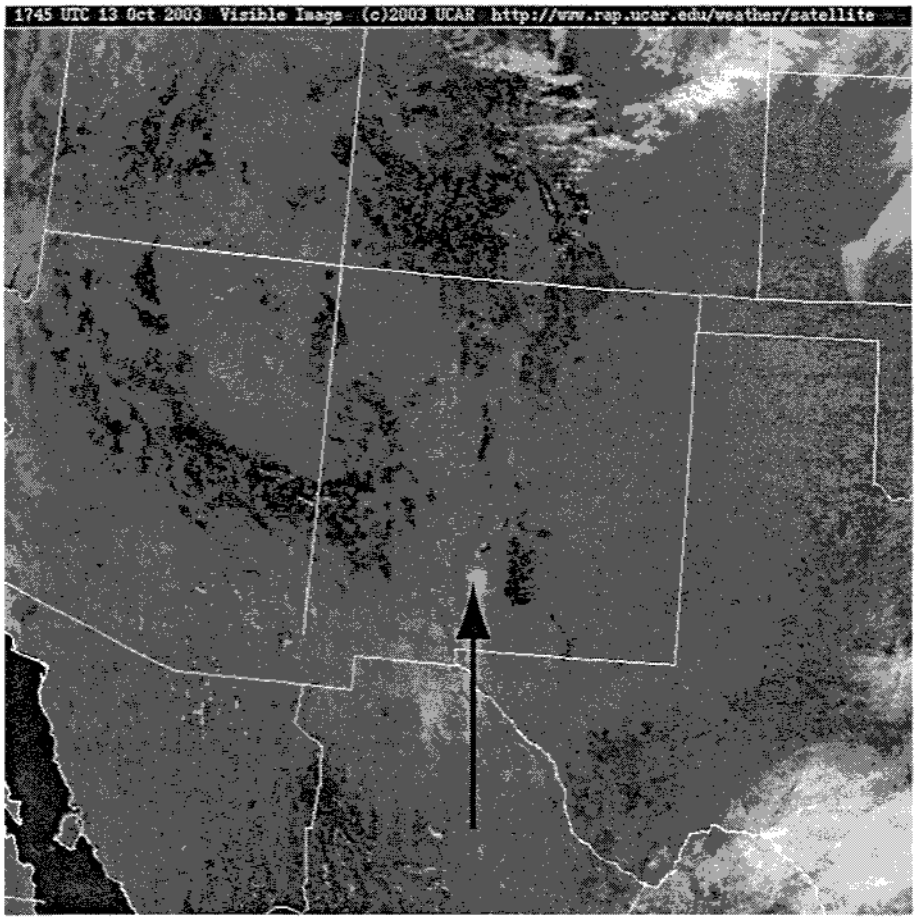

Figure 2.6. Visible satellite image from late morning local time from 13 October 2003 over the southwestern USA. Note the white spot in south-central New Mexico, as indicated by the arrow, which shows the location of the white sands that cover the ground over a relatively large area. © 2006 University Corporation for Atmospheric Research, used with permission.

why White Sands, New Mexico, is so easy to see in visible satellite images (Fig. 2.6). Albedo also is influenced by the vegetation type and coverage, and changes throughout the vegetation life cycle (Moore *et al.* 1996). The angle of incidence also can have a large effect on the albedo, especially for water surfaces. Anyone who enjoys boating or water sports knows that a lot of sunlight is reflected by the water when the sun is low on the horizon, and very little when the sun is directly overhead. Waves on the water also affect the albedo.

Snow cover can change the albedo of a surface dramatically in a very short period of time. New snow is very bright and has an albedo close to 1.0. As snow ages, it typically has a lower albedo as dirt gets blown on top of the snow.

However, the interactions between snow and vegetation are complex. Betts and Ball (1997) find an 850 hPa temperature error in the European Center for Medium-range Weather Forecasting (ECMWF) medium-range forecasts over southwestern Canada during the winter. They hypothesize that when snow initially falls on the trees in the coniferous forests, it accumulates on the tree needles. It remains on the needles until the wind begins to blow. The wind causes the snow to fall off the trees and onto the ground below. Thus, the albedo changes from one representing a snow-covered surface to one representing a dark green surface of pine needles over a very short time period. Tests suggest that when the albedo in southwestern Canada is modified to account for the decrease in albedo associated with the falling of snow off the trees, the temperature errors in the forecasts are reduced.

Finally, human beings influence the albedo in a wide variety of ways. Homes, office buildings, parking lots and roads are built that dramatically change the reflective properties of the ground surface. The vegetation and land use of large regions are altered through farming, irrigation, logging, burning, and watering. Chase *et al.* (2001) propose that changes in land use can account for most of the observed surface warming of the past several hundred years. Thus, one could argue that parameterizations are needed for human activities as a component of NWP, at least when examining seasonal or longer timescales. This is already accounted for in global climate models by examining different emission scenarios for greenhouse gases.

2.2.3 Longwave upwelling radiation (Q_{Lu})

Longwave upwelling radiation is the amount of longwave radiation emitted from the Earth's surface. It may be viewed as a continuous electromagnetic spectrum of waves with wavelengths from 4 to 100 μm. Therefore, longwave radiation has very little overlap with the wavelength spectrum associated with incoming solar radiation. Since the intensity of longwave radiation is explained by the Stefan–Boltzmann law, it is influenced most strongly by the temperature of the ground surface and by the value of surface emissivity (the power emitted by a body at temperature T to the power emitted by a blackbody at temperature T). Of course, the ground surface temperature is influenced by incoming solar radiation, albedo, downwelling longwave radiation, soil type, soil moisture, and the temperature of the soil below the ground surface. One can already begin to see the numerous feedbacks in this complex Earth system that sustains life. Vegetation also influences the longwave upwelling radiation, as thick forest canopies can act to retard radiation emitted from the ground via multiple reflectances. The upwelling longwave radiation from

thick forests is determined largely by the temperature and emissivity of the vegetation canopy.

2.2.4 Longwave downwelling radiation (Q_{La})

Longwave downwelling radiation is the amount of longwave radiation emitted from the atmosphere that reaches the ground surface. It is influenced by the atmospheric temperature, especially from the lower levels of the atmosphere. But many other factors influence downwelling longwave radiation. Clouds play a large role, acting to absorb and emit longwave radiation very efficiently. Greenhouse gases, such as carbon dioxide, ozone, and methane also contribute significantly, as does water vapor. Together, the effects of increasing concentrations of greenhouse gases and the feedback due to water vapor constitute the major unresolved questions regarding global warming. Pollution and aerosols also influence the downwelling radiation, although they vary in concentration and in their characteristics from location to location.

2.2.5 Sensible heat flux (Q_H)

Sensible heat flux is the rate of heat transfer per unit area from the ground to the atmosphere. During a typical cloudless summer day, the sensible heat flux increases during the morning hours, reaching a maximum in the early afternoon before decreasing back towards zero after the sun sets (Fig. 2.7). It is most strongly affected by the difference in temperature between the ground (or water) surface and the overlying atmosphere immediately above the ground. However, observations indicate that the conditions throughout the lower atmosphere also play a role, as the heat flux is modified by wind speed, wind shear, and the vertical temperature gradient within the planetary boundary layer. The presence and type of vegetation also influences the sensible heat flux, owing to the height, coverage, and structure of the vegetation affecting the ground and vegetation canopy temperatures, and the low-level wind shear. In very dense canopies, almost all of the sensible heat flux comes from the vegetation layer.

2.2.6 Latent heat flux (Q_E)

Latent heat flux is the rate of moisture transfer per unit area from the ground (or water) surface to the atmosphere. Similarly to sensible heat flux, it is affected by the surface temperature and the temperature, wind speed, wind shear, and stability of the lower levels of the atmosphere. Vegetation plays an even larger

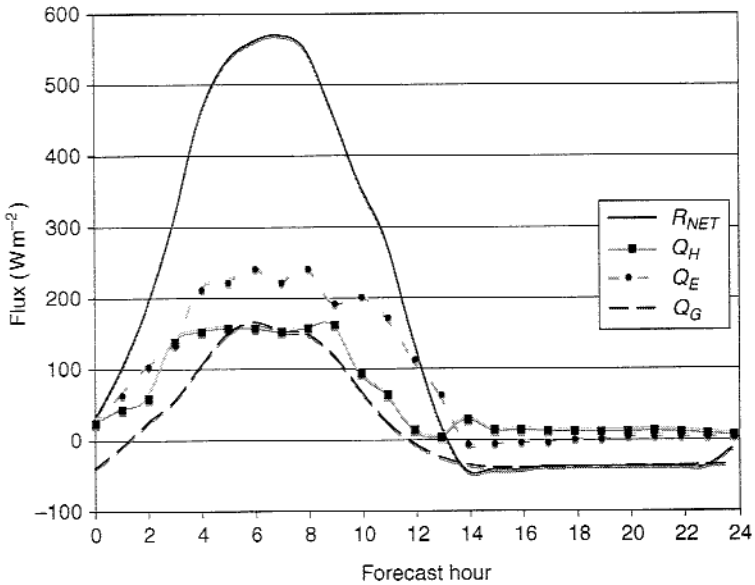

Figure 2.7. Monthly mean diurnal cycle of observed components of the surface energy budget at Norman, Oklahoma, for July 1997. Forecast hour 0 corresponds to 1200 UTC, or 7 a.m. local time. Hourly values of net radiation (R_{NET} is the sum of all four radiation terms), sensible heat flux (Q_H), latent heat flux (Q_E), and ground heat flux (Q_G) are shown. After Marshall *et al.* (2003), where data are from the Oklahoma Mesonet.

role in determining the latent heat flux, as vegetation can transfer moisture from deep soil layers to the atmosphere. Soil type also is important, as water retention differs among the various soil types. And of course, the soil moisture content and the presence of water (lakes, rivers, oceans) are important factors.

A useful parameter for comparing the relative amounts of sensible and latent heat flux is the Bowen ratio (β), defined as the ratio of the sensible to the latent heat fluxes at the surface (Bowen 1926). Over semi-arid regions, the Bowen ratio can exceed a value of 5. Over grasslands and forests, values of 0.5 are typical. Bowen ratios drop to 0.2 over irrigated orchards or grass, and to 0.1 over water. Values of Bowen ratios greater than one correspond to surfaces with more sensible heat flux than latent heat flux, and vice versa when the Bowen ratio is less than one.

As mentioned previously, differences in the relative amounts of sensible and latent heat flux can lead to very different boundary layer depths (Chang and Wetzel 1991; Segele *et al.* 2005), setting limits on whether or not precipitation is likely to occur. In addition, horizontal gradients of sensible and latent heating can enhance the low-level baroclinicity and produce secondary circulations that influence boundary layer structure and convective development

(Lakhtakia and Warner 1987; Chang and Wetzel 1991; Segele *et al.* 2005). These differences can further feed back to the atmosphere and influence rainfall in more distant locations.

2.2.7 *Ground heat flux (Q_G)*

Ground heat flux is the rate of heat transfer from the ground surface into the deeper soil levels. As with the other fluxes from the surface, it is influenced by surface temperature, soil type, soil moisture, and vegetation. Observations suggest that the upper 25 cm of soil has the largest diurnal changes in temperature, with temperature changes in the deeper soil levels occurring much more slowly. However, on yearly timescales, soil temperatures vary at depths below 1.5 m. While the ground heat flux is often smaller in magnitude than the sensible and latent heat fluxes, as shown in Fig. 2.7, it can be comparable in magnitude and is rarely insignificant.

While there are even more processes that affect these terms in the surface energy budget, this discussion provides some perspective on the complexity of the atmospheric system. Many of the processes listed are interrelated, and have complicated interactions, making their prediction very challenging. As a thought experiment, vary one of the variables and see how many terms in the surface energy budget are influenced by changes to just this one variable. It is very likely that most of the terms in the energy budget are influenced by this chosen variable but in different ways. This complexity and interrelatedness is at the heart of the difficulty that weather prediction faces every day. A brief look at how each term of the energy budget is described mathematically follows, building the foundation for a more detailed look at the soil–vegetation–atmosphere parameterization schemes that occurs in Chapter 3 and water–atmosphere parameterizaton schemes that occurs in Chapter 4.

2.3 Net radiation

2.3.1 *Incoming solar radiation*

Incoming solar radiation is often calculated, in its simplest form, using

$$Q_s = S\left(\frac{\bar{d}}{d}\right)^2 (1 - a)\cos(\zeta)\tau_s, \tag{2.1}$$

where ζ is the solar zenith angle, S is the solar irradiance (1365–1374 W m^{-2}), d is the distance from the sun to the Earth, $\bar{d}$ is the mean distance from the sun

to the Earth, a is the albedo, and τ_s is the transmissivity. The $(\bar{d}/d)^2$ term accounts for the elliptical orbit of the Earth around the sun and departs by no more than 3.5% from unity (Liou 1980). The zenith angle is determined from

$$\cos(\zeta) = \sin(\varphi)\sin(\delta) + \cos(\varphi)\cos(\delta)\cos(h), \tag{2.2}$$

where φ is the latitude, δ is the solar declination angle, and h is the local hour of the sun. Note that $h = 0$ at local solar noon, when the sun is directly overhead. The zenith and declination angles are defined and shown graphically in Figs. 2.8 and 2.9, respectively. The declination angle can be calculated as

$$\delta = 23.45^\circ \cos\left[\frac{2\pi(d - d_{solstice})}{d_y}\right], \tag{2.3}$$

where d is the Julian day, $d_{solstice}$ is 173, or the day of the summer solstice, and d_y is 365.25, the average number of days in a year. Finally, the local hour of the sun (h) is defined as

$$h = \frac{(t_{UTC} - 12)\pi}{12} + \frac{\lambda\pi}{180}, \tag{2.4}$$

where t_{UTC} is the coordinated universal time (UTC) in hours (0 to 24), and λ is the longitude (plus for east, minus for west) in degrees. Note that when $\cos(\zeta) < 0$, then $Q_S = 0$ for the sun is below the horizon and there is no solar radiation reaching the ground surface.

The albedo is the fraction (0 to 1) of incoming radiation that is reflected back to space. Values of albedo can range from 0 to near 1 depending upon the land

Figure 2.8. Illustration of the solar zenith angle (ζ), defined as the angle between the direction of a direct beam of radiation from the sun and a line normal to the surface of the Earth.

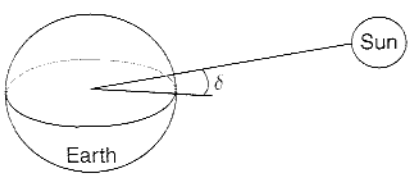

Figure 2.9. Illustration of the declination angle (δ), defined to be the angular distance of the sun north (positive) or south (negative) of the equator when a line is connected between the center of the Earth and the center of the sun.

Table 2.1. *Typical values for albedo for different surface conditions.*

Surface	Albedo
Dark, wet soils	0.05
Coniferous forests	0.10
Grass and agricultural lands	0.20
Light colored soils	0.40
Snow	0.95
Water when sun is directly overhead	0.05
Water when sun elevation angle is low	1.0

surface, and vary most strongly over water. Typical values of albedo are shown in Table 2.1.

The transmissivity term (τ_s) plays a large role in determining the amount of incoming solar radiation. This term incorporates the influences of aerosols, water vapor, and clouds, and as such can be quite complex. A much more complete discussion of it is found in Chapters 8 and 9.

2.3.2 Upwelling longwave radiation

Upwelling longwave radiation is calculated as

$$Q_{Lu} = \varepsilon_g \sigma T_g^4, \tag{2.5}$$

where ε_g is the emissivity, σ is the Stefan Boltzmann constant ($5.67 \times 10^{-8}\,\mathrm{W\,m^{-2}\,K^{-4}}$), and T_g is the temperature (K) of the ground surface. Emissivity values for most surfaces on the Earth range from 0.9 to 0.99, where emissivity is defined as the ratio of the emittance to the emittance expected from a blackbody.

2.3.3 Downwelling longwave radiation

The downwelling longwave radiation from the atmosphere to the Earth's surface is much more complicated to calculate and estimate. It is often calculated using complex radiative transfer models as discussed in Chapters 8 and 9. However, a number of approaches have been developed based upon empirical relationships between the downwelling radiation and various meteorological parameters that are routinely measured. While these approaches are not as accurate as the radiative transfer models, and generally should not be used in

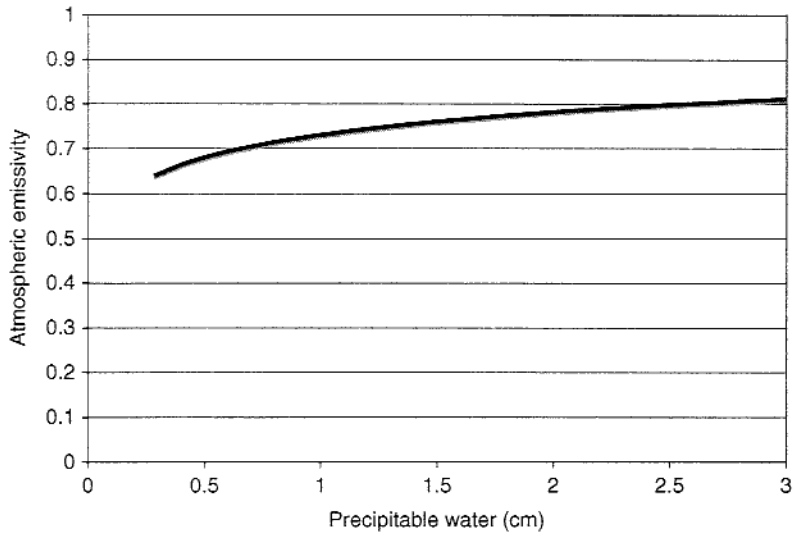

Figure 2.10. Atmospheric emissivity (ε_a) versus total column precipitable water (cm) using the formula from Monteith (1961).

numerical weather prediction models today, they provide a good summary of what is important in the calculation of downwelling radiation. For example, under clear skies Monteith (1961) finds that

$$Q_{Ld} = \varepsilon_g \varepsilon_a \sigma T_a^4, \tag{2.6}$$

where T_a is the air temperature (K) at approximately 40 hPa above ground level, w_p is the total column precipitable water (cm), and ε_a is the atmospheric emissivity, defined as

$$\varepsilon_a = 0.725 + 0.17 \log_{10}(w_p). \tag{2.7}$$

The empirical relationship expressed by (2.6) and (2.7) only considers the temperature 40 hPa above the ground because, in general, more than half the radiant flux received at the ground from the atmosphere comes from gases in the lowest 100 m and roughly 90% from gases within the lowest 1 km. Thus, the emissivity of the air increases in tandem with increasing total column precipitable water as shown in Fig. 2.10.

Typically, clouds dense enough to cast a shadow on the ground emit as a blackbody at the temperature of the water droplets or ice crystals from which they are formed. Clouds strongly affect Q_{Ld} since they emit in the 8–13 μm waveband, called the atmospheric water vapor window, since other absorbers are generally not present in this band. Since most of the atmospheric radiation reaching the surface is emitted from below the cloud base, and the cloud base is

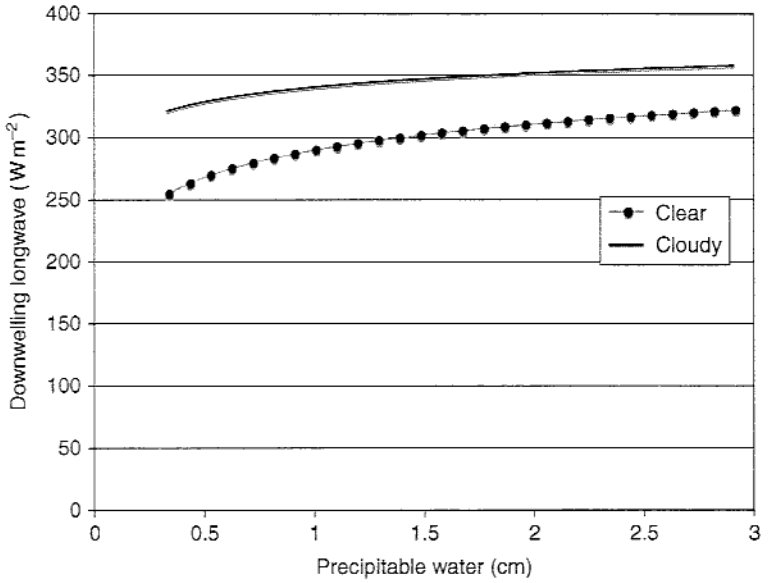

Figure 2.11. Calculated downwelling longwave radiation (W m^{-2}) versus the total column precipitable water (cm) for clear (gray line) and 60% cloudy skies (black line) using the formula in (2.8). The air temperature is assumed to be 290 K and cloud base temperature is assumed to be 270 K.

located most often above 1 km, it is possible to treat the gaseous component of downward radiation separately from the cloud component. One approach that is used in simple radiation schemes is

$$Q_{Ld} = \varepsilon_g \varepsilon_a \sigma T_a^4 + b\varepsilon_g (1 - \varepsilon_a)\sigma T_c^4, \tag{2.8}$$

where b is the cloud fractional area (0 to 1), ε_a is the atmospheric emissivity, and T_c is the temperature of the base of the cloud. The first term on the right-hand side represents the clear sky contribution, with the second term acting to increase the downwelling radiation due to clouds. Assuming an air temperature of 290 K and a cloud temperature of 270 K with 60% cloud cover, the downwelling longwave radiation reaching the surface is enhanced by 11–26% due to the clouds (Fig. 2.11). Cloud cover clearly plays a greater role in the amount of downwelling radiation when the atmospheric precipitable water is low, although clouds do not form unless there is sufficient moisture to reach saturation. Other simple models use a slightly different approach, such as

$$Q_{Ld} = Q_{Ld_{clear}}(1 - b) + bQ_{Ld_{overcast}}, \tag{2.9}$$

where $Q_{Ld_{clear}}$ is defined similarly to (2.6). Alternatively, one can add enhancements to $Q_{Ld_{clear}}$ by dividing the clouds into layers, such as

$$Q_{Ld} = Q_{Ld_{clear}}\left(1 + \sum_{i=1}^{3} c_i n_i\right), \tag{2.10}$$

where n_i is the fractional cloudiness within a specific atmospheric layer, say the surface to 850 hPa for layer 1, and c_i is an enhancement coefficient.

When one considers how cloud sizes are related to grid spacing in models, it is apparent that most models in use today need a parameterization for downwelling radiation that includes a representation of clouds. Since cumulus clouds, for instance, can be 500 m or less in width, it is likely that all models with a grid spacing greater than 200 m need some subgrid cloud cover scheme; otherwise these smallest and frequently observed clouds are not represented in the model.

2.4 Sensible heat flux

Before getting into too many details about how to determine the sensible heat flux, it is wise to review the definition of flux. Flux is a rate of flow, or the transfer of a quantity per unit area per unit time. Thus, flux F can be written as

$$F = -u_T(\bar{X}_{top} - \bar{X}_{bottom}), \tag{2.11}$$

where u_T is a transport velocity or conductivity. Thus, flux depends upon the change in the quantity of interest (X) across the zone over which the flux is calculated (top bottom) and the speed of the transport (u_T).

In fields outside of meteorology, fluxes are often viewed from a slightly different framework. To understand this framework one must recall Ohm's law from an introductory physics class. This law states that for a given conductor, at a given temperature, the current (I) is directly proportional to the difference of potential (voltage) between the ends of the conductor, such that

$$\text{current} = \frac{\text{voltage}}{\text{resistance}}. \tag{2.12}$$

Thus, the larger the resistance (R) becomes, the smaller the current that results from a given voltage. As is seen later, this basic resistance framework for defining current can be used to define surface sensible and latent heat fluxes as well. Note that any combination of resistances can always be replaced by a single, equivalent value of resistance.

Resistors in a parallel circuit are illustrated in Fig. 2.12, and lead to the relationship

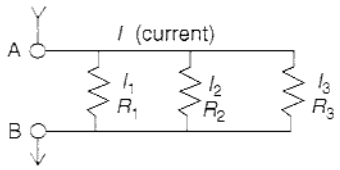

Figure 2.12. Illustration of a parallel circuit with three resistors (R_1, R_2, and R_3) and three different currents (I_1, I_2, and I_3).

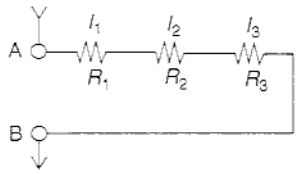

Figure 2.13. Illustration of a series circuit with three resistors (R_1, R_2, and R_3) and the same current across each resistor (I_1, I_2, and I_3).

$$\frac{1}{R} = \frac{1}{R_1} + \frac{1}{R_2} + \frac{1}{R_3}, \tag{2.13}$$

where R is the total resistance and R_1, R_2, and R_3 are the resistances of the individual resistors. Here the voltage is the same across each resistor, which leads to the three currents being defined as

$$I_1 = \frac{V_{AB}}{R_1}, \qquad I_2 = \frac{V_{AB}}{R_2}, \qquad I_3 = \frac{V_{AB}}{R_3}, \tag{2.14}$$

and the total current I equals

$$I = I_1 + I_2 + I_3 = V_{AB}\left(\frac{1}{R_1} + \frac{1}{R_2} + \frac{1}{R_3}\right). \tag{2.15}$$

In contrast, for resistors in a series circuit we have the situation illustrated in Fig. 2.13, where the total resistance is the sum of the individual resistances, such that

$$R = R_1 + R_2 + R_3. \tag{2.16}$$

In a series circuit, the current is the same across each resistor, such that

$$V_{AB} = V_1 + V_2 + V_3 = IR_1 + IR_2 + IR_3 = I(R_1 + R_2 + R_3). \tag{2.17}$$

A few simple examples can be used to highlight the factors that influence the value of the resistance. It is well-known that all metals have a specific

Voltage	=	Current	*	Resistance
$\Delta T = T_2 - T_1$	=	Fluxes $Q_H\ Q_E\ Q_G$	*	??

Figure 2.14. An illustration of the relationship between electric voltage and current, and temperature (or moisture) differences and fluxes.

resistance, so if one takes a wire of a given length l and doubles the length to $2l$, then what happens to the resistance? Since the length of the wire is doubled, it is as though two wires of length l are added together in series. Thus, the resistance doubles, indicating that $R \propto$ length. If instead the cross-sectional area of the wire is doubled, then what happens to the resistance? In this case it is like two identical wires being welded together, and the wires are in parallel. Thus, R is reduced by a factor of 2, indicating that $R \propto 1/\text{area}$. Combining these two relations yields $R \propto$ length/area. Since numerical weather prediction models typically define heat flux per square meter, the resistance is only a factor of length – the distance from the ground surface to the first model level. This distance can play a large role in how well the model responds to surface forcing.

It may not yet be obvious how this relates to meteorology and the calculation of the sensible heat flux. One finds that there are analogous relationships between the temperature or moisture difference between the ground surface and the atmosphere, and the electric voltage between two points on a circuit, and also between the electric current and fluxes (Fig. 2.14). However, these analogies lack the precise information needed to calculate the sensible heat flux. Instead, a well-known physical process is used as the basis for deriving an expression for the sensible heat flux.

We know that for conduction, the transport of energy occurs solely as a consequence of the random motion of individual molecules, so the heat flux Q_H in the vertical direction is given by

$$Q_H = -k_a \frac{\partial T}{\partial z}, \tag{2.18}$$

where k_a is the thermal conductivity of air ($\mathrm{W\,m^{-1}\,K^{-1}}$). By analogy, one can assume that the vertical heat flux due to turbulent eddies behaves similarly. So, we define a thermal diffusivity (κ), which is equivalent to the thermal conductivity in (2.18) but with the heat transfer being due to turbulence instead of conduction, such that

$$\kappa = \frac{k_a}{\rho c_p}, \tag{2.19}$$

where ρ is the air density and c_p is the specific heat at constant pressure. Note that diffusivity can simply be viewed as another name for a transfer coefficient, such that

$$\overline{w'T'} = -\kappa \frac{\partial \bar{T}}{\partial z}, \tag{2.20}$$

where κ has units of $m^2 s^{-1}$. This expression defines a flux-gradient relationship. If one assumes that temperature varies only in the vertical direction, (2.18) can be rewritten for heat conduction due to turbulent eddies as

$$dT = -\frac{Q_H}{k_a}\, dz = -\frac{Q_H}{\rho c_p}\frac{dz}{\kappa}. \tag{2.21}$$

Recall that resistance is proportional to length divided by area, and that resistance must always be defined over a specified length. If Q_H is assumed to be constant in the surface layer over which the flux is calculated, which is a reasonable assumption, then

$$\int_{T_1}^{T_2} dT = -\int_{z_1}^{z_2} \frac{Q_H}{\rho c_p}\frac{dz}{\kappa} = -\frac{Q_H}{\rho c_p}\int_{z_1}^{z_2}\frac{dz}{\kappa} = -\frac{Q_H}{\rho c_p} r_H, \tag{2.22}$$

where r_H is defined as the resistance to heat flux. Resistance has units that are the inverse of velocity ($s\,m^{-1}$). Resistance depends upon the separation distance over which the flux is determined, so that the model vertical grid spacing becomes very important in determining the resistance over the lowest model layers. In fact, all other things being equal, the thicker the lowest model layer is the larger the resistance, and the slower the response of the model to surface heating. This is one very important way in which the model vertical grid influences directly the physical process parameterization schemes. Rearranging (2.22), the expression for sensible heat flux written in resistance form is

$$Q_H = \frac{\rho c_p \Delta T}{r_H}, \tag{2.23}$$

where $\Delta T = T(z_1) - T(z_2)$ is the temperature difference across a layer of the atmosphere, $r_H > 0$ is the resistance across this same layer, and $z_2 > z_1$. Typically, for the sensible heat flux calculations in numerical models, the layer over which the heat flux is calculated is from the ground surface to the lowest model level so that $z_1 = 0$ and z_2 is some positive value determined by the model vertical grid spacing. When the ground temperature is warmer than the air temperature, then $\Delta T > 0$ and $Q_H > 0$. Note that some investigators prefer to use conductance g instead of resistance where $g \equiv 1/r_H$ (e.g., Cox *et al.* 1998).

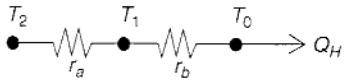

Figure 2.15. Illustration of three different temperatures ($T_2 > T_1 > T_0$), separated by air with resistances r_a and r_b, and with flux Q_H.

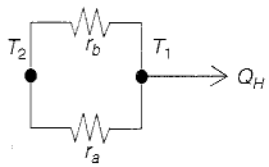

Figure 2.16. Illustration of two different temperatures ($T_2 > T_1$), separated by air or vegetation with resistances r_a and r_b, and with flux Q_H.

Now for a few examples of how sensible heat flux is calculated for various situations. First, if the resistances are in series and the flux is constant, i.e. no losses or gains occur along the path, then the situation is as shown in Fig. 2.15, indicating that

$$Q_H = \frac{\rho c_p (T_2 - T_1)}{r_a} = \frac{\rho c_p (T_1 - T_0)}{r_b} = \frac{\rho c_p (T_2 - T_0)}{r_a + r_b} = \frac{\rho c_p (T_2 - T_0)}{r_{total}}. \quad (2.24)$$

Resistances in a series configuration occur, for example, when the sensible heat flux from the ground surface interacts first with a vegetation layer and then with the atmosphere. If the resistances are in parallel, then the situation is as shown in Fig. 2.16, indicating that

$$\begin{aligned} Q_H &= \frac{\rho c_p (T_2 - T_1)}{r_a} + \frac{\rho c_p (T_2 - T_1)}{r_b} = \rho c_p (T_2 - T_1)\left(\frac{1}{r_a} + \frac{1}{r_b}\right) \\ &= \frac{\rho c_p (T_2 - T_1)}{\bar{r}}, \end{aligned} \quad (2.25)$$

where

$$\bar{r} = \left(\frac{1}{r_a} + \frac{1}{r_b}\right)^{-1}. \quad (2.26)$$

Resistances in parallel occur, for example, when both sides of a leaf interact with the atmosphere to transfer water from the plant to the atmosphere. Putting these two scenarios together, then if both parallel and series resistors are found (Fig. 2.17), the heat flux equals

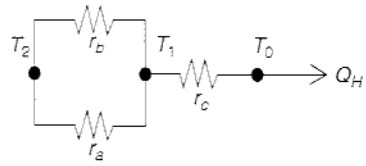

Figure 2.17. Illustration of three different temperatures ($T_2 > T_1 > T_0$), separated by air or vegetation with resistances r_a, r_b and r_c, and with flux Q_H.

$$Q_H = \frac{\rho c_p (T_2 - T_0)}{\bar{r} + r_c}. \tag{2.27}$$

where the parallel resistances r_a and r_b are replaced by a single resistance $\bar{r}$ as shown earlier.

Resistors in series occur in the equations for both sensible and latent heat flux, as the resistances are calculated from the ground surface to the atmospheric layer within the vegetation canopy, and then from this canopy layer to the atmospheric layer above the canopy. Resistors in parallel also occur in the sensible and latent heat flux equations when there are flux contributions from both bare soil and vegetated surfaces within the same model grid cell. Thus, the scenario shown in Fig. 2.17, and the expression for heat flux in (2.27), are representative of how heat fluxes are defined in a resistance formulation within many models.

Similar to the derivation of the resistance form of the sensible heat flux equation, as shown in (2.18)–(2.23), one can derive resistance equations for the other surface flux terms in the surface energy budget as well. Thus, there are diffusivities for momentum (eddy viscosity), heat (eddy conductivity), and water vapor (eddy diffusivity), and for other variables that are influenced by turbulent motions, such as carbon dioxide, ozone, and methane. The various diffusivities are shown in Table 2.2.

While the resistance to heat flux r_H has been defined, it has not yet been expressed mathematically. In earlier meteorological models, heat flux is typically calculated in terms of bulk transfer coefficients that are multiplied by the wind speed. Even from everyday experiences of living and breathing within the atmospheric surface layer, the lowest 10–40 m above ground level, it is clear that wind gusts act to remove the hotter air that develops near the ground. Thus, intuition suggests that the resistances used in the calculations of sensible and latent heat fluxes should be related to the wind speed. But how are these resistances calculated? The process begins by calculating the momentum flux, from which everything else follows.

The goal is to calculate the resistance to momentum flux r_M within the atmospheric surface layer, since this defines the momentum flux τ and sets

Table 2.2. *Definitions of various fluxes and the variables used to define the diffusivities used in the calculations of resistance. Remember that while the values of diffusivity are assumed to be constant over a given location, the values of resistance change as the layer over which the flux is calculated changes.*

Variable	Flux	Diffusivity
Temperature (T)	$Q_H = \frac{\rho c_p \Delta T}{r_H}$	κ
Specific humidity (q)	$Q_E = \frac{\rho L_v \Delta q}{r_V}$	D_v
Wind speed (V)	$\tau = \frac{\rho \Delta V}{r_M}$	ν

the stage for the other resistance calculations. Close to the ground we know from the kinetic theory of gases that for laminar flow

$$\tau = \nu \frac{\partial}{\partial z}(\rho \bar{u}), \tag{2.28}$$

which states that the stress is directly proportional to the wind speed gradient. This is valid in the lowest few millimeters above z_0, the roughness height, where the mean wind speed goes to zero and molecular processes are dominant.

It is assumed that the same equation can be generalized to turbulent flow, such that

$$\tau = K_m \frac{\partial}{\partial z}(\rho \bar{u}), \tag{2.29}$$

where K_m is an eddy viscosity ($\sim 1\ \mathrm{m^2\ s^{-1}}$). This expression again defines a flux-gradient relationship. One important difference between these two equations for momentum flux, (2.28) and (2.29), is that while ν is constant for a given p and T, K_m varies depending upon the surface roughness, buoyancy forces, and the height above the ground.

At this point, some insight into the behavior of the atmosphere is needed to decide how best to proceed. What is known observationally that could help to determine the momentum flux or stress? Observations and scaling analyses show that in neutral planetary boundary layers, where the potential temperature is constant with height and the sensible heat flux is zero, one finds the relationship

$$\frac{\bar{u}(z)}{u_*} = \frac{1}{k} \ln\left(\frac{z}{z_0}\right). \tag{2.30}$$

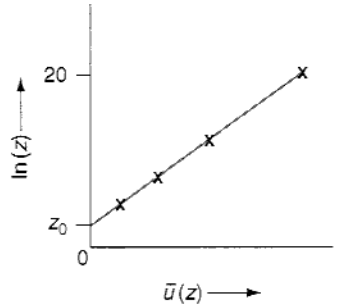

Figure 2.18. Illustration of the log wind profile, where the crosses are observed mean wind speeds.

This famous expression is called the log wind profile. Here k is von Karman's constant ($\sim$0.4), u_* is the friction velocity ($\mathrm{m\,s^{-1}}$), and z_0 is the roughness length (m). The log wind profile is a characteristic change of wind speed with height that is observed under neutral stability conditions across the globe. When the wind speed is plotted versus the natural logarithm of the height of the observation, a straight wind speed profile is found (Fig. 2.18). One of the key parameters for this wind profile is the roughness length, z_0, the height above ground at which the mean wind speed goes to zero. By taking the derivative of (2.30) with respect to z, the log wind profile specifies that

$$\frac{\partial \bar{u}}{\partial z} = \frac{u_*}{kz}. \tag{2.31}$$

Thus, the change in wind speed with height is inversely proportional to the height above ground level of the observation, and the wind speed changes most rapidly just above the ground and more slowly as the height increases.

Numerous observational studies have evaluated the log wind profile and calculated the roughness length over various surfaces. Results indicate that over ice or smooth water the roughness length can be as small as 10^{-4} m, while over forests or cities the roughness length can be as large as several meters. A crude estimate for the roughness length is obtained using $z_0 \sim h/8$, where h is the height of the vegetation. Table 2.3 summarizes some of these results to illustrate the variations in roughness length that are observed.

Returning to (2.29), the equation for momentum flux that started the hunt for an expression for r_M, and assuming that ρ is a constant throughout the layer in which the log wind profile is observed, one finds that the momentum flux can be written as

$$\tau = \rho K_m \frac{\partial \bar{u}}{\partial z}. \tag{2.32}$$

Table 2.3. *Roughness lengths measured over various surface types.*

Surface	Roughness length (m)
Ice	10^{-4}
Grass (mown)	10^{-2}
Long grass, rocky ground	0.05
Pasture	0.20
Suburban housing	0.6
Forests, cities	1–5

Knowing that $u_*^2 = (\tau/\rho)$ and assuming that u_* is a constant, one can rearrange a few terms to get an expression for the eddy viscosity,

$$K_m = \frac{(\tau/\rho)}{(\partial\bar{u}/\partial z)} = \frac{u_*^2}{(u_*/kz)} = u_* kz. \tag{2.33}$$

Therefore, using the equation for momentum stress in resistance form from Table 2.2, one can arrive at an equation for the momentum resistance r_M, such that

$$r_M = \frac{\rho\Delta u}{\tau} = \frac{\rho\Delta u}{\rho K_m(\partial\bar{u}/\partial z)} = \frac{\Delta\bar{u}}{u_* kz(\Delta\bar{u}/\Delta z)} = \frac{\Delta z}{u_* kz}. \tag{2.34}$$

When integrated from the ground to the top of the surface layer in question (and in which the log wind profile generally is valid), this becomes

$$r_M = \int_{z_0}^{z} \frac{dz}{u_* kz} = \frac{1}{u_* k}\ln\left(\frac{z}{z_0}\right) \equiv \frac{1}{u_* k}\ln\left(\frac{z_{eff}}{z_0}\right), \tag{2.35}$$

where z_{eff} is the effective height. Finally, then, we have a mathematical expression for the resistance to momentum transfer!

Before moving on, there are a few things that need to be mentioned. First, recall that resistance is always defined over a particular depth as indicated in (2.35). As the thickness of model layers changes, the resistance also changes. Second, the use of the variable z_{eff} in (2.35) is a relatively standard form of the equation. The effective height is due to the observation that some roughness elements when packed close together, such as forest canopies, act like a displaced ground surface. This typically only occurs over a fairly uniform forest canopy or in urban areas with relatively high-density housing. In this case, the flow behaves as though the ground surface has been raised upward to near the height of the tree or house tops. Although the log wind profile is still observed, its apparent origin is moved upward to a height d above the ground

surface. The effective height is defined as $z_{eff} = z - d$ to account for this displacement when needed. The exact height of d for a given canopy depends upon how the drag force is distributed through the foliage, and the structure of the mean wind and turbulence within the canopy. In general, a value of d representing a height that is 75% of the average canopy height seems to work well (Kaimal and Finnigan 1994). For most applications, $d = 0$ is used in the calculations.

In completing this derivation of the resistance, several assumptions are used that are true within the atmospheric surface layer. Remember that the surface layer is a "thin resistor" where fluxes of sensible heat, latent heat, and momentum change by less than 10%. Typically the surface layer is less than 50 m deep during the daytime and less than 20 m deep at night. The assumptions made are that the mean motion is one-dimensional (no horizontal fluxes are important), the Coriolis force can be neglected, the shearing stress and pressure gradient force can be neglected with respect to the viscous force, and the mixing length depends upon the distance of the fluid from the boundary (see Munn 1966).

Complications arise because the atmosphere is not often neutral within the surface layer. Thus, the standard form of the log wind profile,

$$\bar{u}(z) = \frac{u_*}{k} \ln\left(\frac{z}{z_0}\right) = \frac{u_*}{k} \ln\left(\frac{z_{eff}}{z_0}\right) = \frac{u_*}{k} \ln\left(\frac{z-d}{z_0}\right), \tag{2.36}$$

is not valid very often. In cases for which the surface layer is unstable or stable, observations indicate that the actual wind profile varies from the values it takes under neutral conditions (Fig. 2.19). The wind speeds are greater than those found under neutral conditions for unstable conditions and less than those found under neutral conditions for stable conditions. Thankfully,

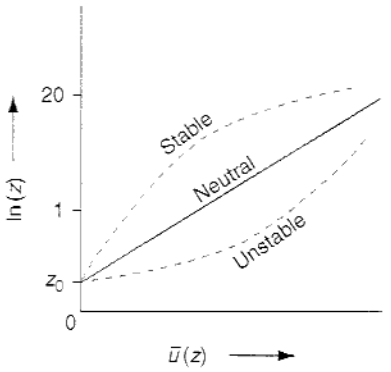

Figure 2.19. Illustration of the typical wind profiles observed under stable, unstable, and neutral conditions. The log wind profile is the wind profile for neutral conditions.

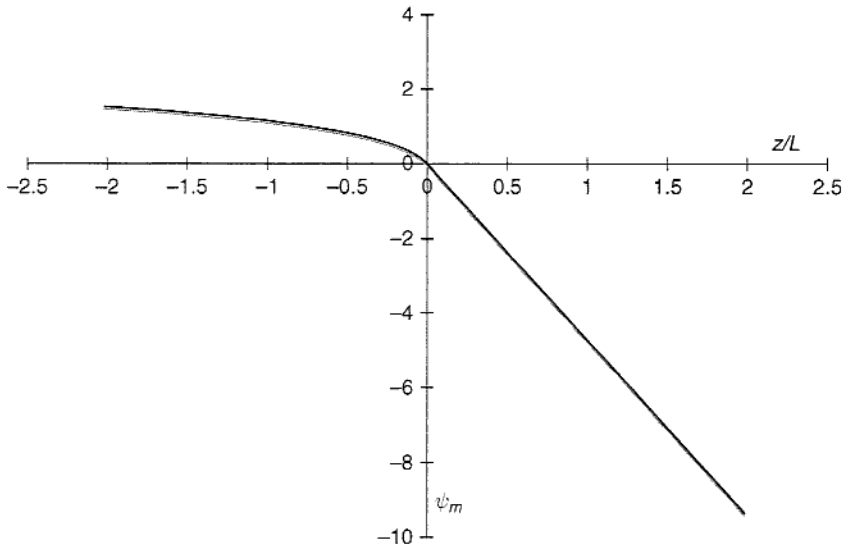

Figure 2.20. ψ_m plotted as a function of z/L, where L is the Monin–Obukhov length. Values of $z/L < 0$ are for unstable conditions, while those of $z/L > 0$ are for stable conditions.

observational results indicate that empirical corrections can be made to the log wind profile to account for departures from neutral stability and that these apply in a variety of locations (Dyer 1963, 1974; Businger *et al.* 1971). The form of this correction (Fig. 2.20) is

$$\bar{u}(z) = \frac{u_*}{k}\left[\ln\left(\frac{z_{eff}}{z_0}\right) - \psi_m\left(\frac{z_{eff}}{L}\right)\right], \tag{2.37}$$

where L is the Monin–Obukhov length. For stable conditions ($L > 0$), the ratio z_{eff}/L represents the relative suppression of mechanical turbulence by the stratification, and

$$\psi_m = -\frac{4.7 z_{eff}}{L} < 0. \tag{2.38}$$

For unstable conditions ($L < 0$), the ratio $-z_{eff}/L$ represents the relative importance of buoyant convection in comparison to mechanical turbulence (Panofsky and Dutton 1984), and

$$\psi_m = 2\ln\left(\frac{1+x}{2}\right) + \ln\left(\frac{1+x^2}{2}\right) - 2\tan^{-1}(x) + \frac{\pi}{2} > 0, \tag{2.39}$$

where

$$x = \left(1 - 15\frac{z_{eff}}{L}\right)^{1/4} \tag{2.40}$$

and

$$L = -\frac{\bar{\theta}_v u_*^3}{kg(\overline{w'\theta'_v})_{sfc}}. \tag{2.41}$$

The Monin–Obukhov length L is generally small and negative on strongly convective days ($L \sim -10$ m), is likely near -100 m on days with strong winds and some solar heating, and is positive and very large for days with mostly mechanically generated turbulence (Panofsky and Dutton 1984).

This correction to the log wind profile produces an alteration to the equation for momentum resistance, such that the resistance to momentum for both neutral and non-neutral surface layers is expressed as

$$r_M = \frac{1}{ku_*}\left[\ln\left(\frac{z_{eff}}{z_0}\right) - \psi_m\left(\frac{z_{eff}}{L}\right)\right]. \tag{2.42}$$

A brief examination of (2.42) and Fig. 2.20 shows that the effect of turbulent flux generally is to reduce r_M during the day and to increase r_M at night. This makes physical sense, since the effects of turbulent motions from strong heating of the ground are expected to produce stronger mixing, and hence greater heat flux. In contrast, when conditions are stable and the turbulence from buoyancy is greatly reduced, the heat flux should be relatively small.

It is important to be aware that other forms of this correction to the log wind profile under non-neutral conditions are given in the literature (e.g., Swinbank 1968; Zilitinkevich and Chalikov 1968; Lobocki 1993) and generally yield similar behaviors. Yaglom (1977) suggests that the differences in these various formulations are due to instrumentation and measurement error. However, the different formulations yield different values of ψ_m that influence the low-level wind speed profiles.

Now that an expression for the resistance to momentum has been derived, which applies for neutral, unstable, and stable boundary layer environments, it can be used to help derive an equation for the resistance to heat flux. Recall that the resistance form of the sensible heat flux equation is

$$Q_H = \frac{\rho c_p (T_{z_a} - T_{z_b})}{r_{H(a,b)}}, \tag{2.43}$$

where z_a and z_b are two specified vertical levels. When calculating the sensible heat flux from the ground surface to the atmosphere, T_{z_a} is often assumed to be equal to the ground temperature (T_g) and T_{z_b} is often assumed to be equal to the air temperature. Thus, the temperature difference in the numerator of (2.43) is

the difference between the ground temperature and the temperature of the closest model level to the ground surface. This suggests, and observations also indicate, that the "origin" of the heat flux lies somewhere below the origin for momentum flux, which occurs at the height of the roughness length z_0 (e.g., Garratt and Hicks 1973; Blyth and Dolman 1995). This changes the depth over which the resistance is calculated when compared to the momentum resistance.

As discussed by Garratt (1992), the transfer of momentum very close to the ground surface is influenced by pressure fluctuations in the turbulent wakes that occur behind the roughness elements. However, for heat transfer no such dynamical mechanism exists to transfer the heat, so the heat is transferred by molecular diffusion across the layer from the surface to the height where turbulence processes dominate. This layer is called the interfacial sublayer and plays an important role in controlling the sensible and latent heat fluxes. The interfacial sublayer is located between the ground surface and the surface layer.

For neutral conditions, it is assumed that $r_M = r_H = r_V$ over the same depth, such that

$$r_{H(z,z_0)} = \frac{1}{ku_*} \ln\left(\frac{z_{eff}}{z_0}\right), \tag{2.44}$$

which is valid from height z down to z_0. However, as is shown later, this expression does not account for the resistance within the interfacial sublayer that must be accounted for in the resistance calculations for heat flux. For non-neutral conditions, observations again suggest that corrections can be made (Paulson 1970), yielding an expression very similar to the resistance to momentum, such that

$$r_{H(z,z_0)} = \frac{1}{ku_*}\left[\ln\left(\frac{z_{eff}}{z_0}\right) - \psi_h\left(\frac{z_{eff}}{L}\right)\right], \tag{2.45}$$

where

$$\psi_h = 2\ln\left[\frac{(1+x^2)}{2}\right] \qquad \text{for} \quad L<0 \tag{2.46}$$

and

$$\psi_h = -\frac{4.7z}{L} \qquad \text{for} \quad L>0, \tag{2.47}$$

where x in (2.46) is defined by (2.40). As with the equations for ψ_m, several versions of the equations for ψ_h are available in the literature and yield similar

differences in the actual values of ψ_h as discussed earlier for ψ_m (see Yaglom 1977). Weidinger *et al.* (2000) indicate that the use of different functions for ψ_h can result in important differences in the surface flux calculations.

Now that a corrected equation for the resistance to heat flux has been derived for both neutral and non-neutral conditions within the surface layer, it is time to account for the additional resistance that occurs in the interfacial sublayer between z_0, the roughness length for momentum flux, and the lower roughness length for heat flux, which is denoted as z_{0h}. Note that

$$\ln\left(\frac{z_{eff}}{z_{0h}}\right) = \ln\left(\frac{z_{eff}}{z_0}\right) + \ln\left(\frac{z_0}{z_{0h}}\right). \tag{2.48}$$

and therefore one finds that

$$r_H = \frac{1}{ku_*}\left[\ln\left(\frac{z_{eff}}{z_0}\right) - \psi_h\left(\frac{z_{eff}}{L}\right)\right] + \frac{1}{ku_*}\ln\left(\frac{z_0}{z_{0h}}\right) = r_a + r_b \tag{2.49}$$

represents the total resistance to sensible heat flux from the surface to height z for both neutral and non-neutral conditions, where r_b is the added resistance of the interfacial sublayer.

Typically, evidence suggests that $z_{0h} \ll z_0$ (Garratt and Hicks 1973). Unfortunately, it still is not clear how one calculates z_{0h}. Several possibilities for the determination of z_{0h} are shown by Garratt and Hicks (1973) and are supported by observations, namely

$$z_{0h} = \frac{z_0}{7} \tag{2.50}$$

or

$$z_{0h} = \frac{\alpha\kappa_m}{ku_*}. \tag{2.51}$$

where $\kappa_m = 0.18 \times 10^{-4}\,\mathrm{m^2\,s^{-1}}$ is the molecular thermal diffusivity of air and α is a fudge factor that is typically set to 1. It also is advocated that z_{0h} should depend upon the sensible heat flux, canopy height, vegetation biomass, incoming solar radiation, or perhaps the local flow conditions (Brutsaert 1982; Garratt 1992; Kubota and Sugita 1994). Zilitinkevich (1995) proposes that the ratio of the two roughness lengths should depend upon the roughness Reynolds number (Re^*), such that

$$\frac{z_0}{z_{0h}} = \exp(kC\sqrt{Re^*}). \tag{2.52}$$

where C is a constant, assumed by Chen *et al.* (1997) to be 0.1, and

$$Re^* = \frac{u_* z_0}{\nu}. \tag{2.53}$$

Chen *et al.* (1997) suggest that this formulation of z_{0h} is most useful, since it allows for variability in the roughness length for heat as a function of the atmospheric flow conditions. Hopwood (1995) suggests that the ratio of z_0 / z_{0h} is near 80 for inhomogeneous, vegetated surfaces, indicating that a substantial variability in z_{0h} needs to be included in models.

For model grid cells that contain a mixture of bare ground and sparse vegetation, Blyth and Dolman (1995) show using a dual-source model, which solves the energy balance over vegetation and soil separately, that the value of z_{0h} used in a model that combines the vegetation and soil components (as is true in many numerical atmospheric models) is dependent upon the humidity deficit, the available energy, the vegetation fraction, and the surface resistance of soil and vegetation. They further show that errors in the estimated values of z_{0h} from single-source models can be as large as a factor of 30! This error has a larger influence on the resistance calculations as the roughness length increases, and can produce errors in the resistance values of over 20%. This result argues for smaller grid spacing in models, in order to have each grid cell contain only bare ground or only vegetation. However, the computational cost of such a grid would be prohibitive. An alternative is the use of subsections, or tiles, within each model grid cell that represent the major vegetation types observed and upon which fluxes are calculated individually for each vegetation type before being combined to a single flux for the entire grid cell. However, it is not certain how often these large errors in the estimated values of z_{0h} occur. As emphasized by Zeng and Dickinson (1998), there is no generally accepted guidance available on how to provide a priori estimates of z_{0h} over heterogeneous surfaces for use in numerical modeling. Further research on this important question is certainly warranted.

2.5 Latent heat flux

Similarly to the calculation of sensible heat flux, the latent heat flux, or moisture flux, is defined as

$$Q_E = \frac{\rho L_v (q_{z_a} - q_{z_b})}{r_{V(a,b)}}, \tag{2.54}$$

where L_v is the latent heat of vaporization, and z_a and z_b again refer to specific heights over which the flux is calculated. Often one would prefer to use vapor pressure instead of specific humidity. We know that

$$q \approx \frac{0.622e}{p}, \tag{2.55}$$

where the vapor pressure term in the denominator is neglected. Using this approximation, one can derive

$$Q_E = \frac{\rho c_p (e_{z_a} - e_{z_b})}{r_{V(a,b)}\gamma}, \tag{2.56}$$

where

$$\gamma = \frac{c_p p}{0.622 L_v} \approx 0.66 \text{ hPa K}^{-1}, \tag{2.57}$$

and the total resistance to latent heat flux under both neutral and non-neutral conditions is

$$r_{V(0,z_{eff})} = \frac{1}{ku_*}\left[\ln\left(\frac{z_{eff}}{z_0}\right) - \psi_h\left(\frac{z_{eff}}{L}\right)\right] + \frac{1}{ku_*}\ln\left(\frac{z_0}{z_{0v}}\right). \tag{2.58}$$

No one has determined a correction to the moisture flux owing to non-neutral conditions, likely owing to the difficulties of observing small moisture gradients accurately, and hence it is assumed that the correction to the heat flux equation for non-neutral conditions is good enough to approximate the corrections to the moisture flux. It also is assumed that the "origin" of the moisture flux at height z_{0v} is near the height of the heat flux origin z_{0h}. But what is z_{0v} exactly? The answer is no one really knows for certain and it is an artifact of the derivation. Several options for estimating this quantity have been suggested. The first is that since

$$z_{0h} = \frac{\alpha\kappa}{ku_*}, \tag{2.59}$$

then the roughness length for moisture might be represented by a similar formula, but with the thermal diffusivity κ replaced by the moisture diffusivity D_v, yielding

$$z_{0v} = \frac{\alpha D_v}{ku_*}. \tag{2.60}$$

The second option suggested is that

$$\frac{1}{ku_*}\ln\left(\frac{z_0}{z_{0v}}\right) = \frac{1}{ku_*}\ln\left(\frac{z_0}{z_{0h}}\right)\left(\frac{\kappa}{D_v}\right)^{2/3}, \tag{2.61}$$

where κ/D_v is the ratio of the two diffusivities and equals approximately 0.93.

Selecting (2.61) for representing the additional moisture flux resistance below z_0, one obtains the complete equation for the resistance to moisture flux

$$r_{V(0,z_{eff})} = \frac{1}{ku_*}\left[\ln\left(\frac{z_{eff}}{z_0}\right) - \psi_h\left(\frac{z_{eff}}{L}\right)\right] + \frac{1}{ku_*}\ln\left(\frac{z_0}{z_{0h}}\right)\left(\frac{\kappa}{D_v}\right)^{2/3} = r_a + r_{bv}, \tag{2.62}$$

where r_{bv} is the added resistance of the interfacial sublayer. Then to summarize, for moisture flux we have

$$Q_E = \frac{\rho L_v(q(z_{0v}) - q(z_{eff}))}{r_a + r_{bv}}. \tag{2.63}$$

When examining (2.63), an obvious question is what is $q(z_{0v})$? Is this value of specific humidity at some level just barely above the ground surface measured routinely? What does it indicate? The answer is that this value of specific humidity is not measured and it likely cannot be measured. One could even put forth the argument that no one really knows what it is meant to be. So to be able to calculate moisture flux, an artifact of our inability to measure $q(z_{0v})$ requires that one somehow defines a surface value for q, which leads to

$$Q_E = \frac{\rho L_v(q_S(T_g) - q(z_{eff}))}{r_a + r_{bv} + r_c} = \frac{M\rho L_v(q_S(T_g) - q(z_{eff}))}{r_a + r_{bv}}, \tag{2.64}$$

where $q_S(T_g)$ is the saturation specific humidity at ground temperature T_g, r_c is the canopy resistance, and

$$M = \frac{r_a + r_{bv}}{r_a + r_{bv} + r_c}. \tag{2.65}$$

which is often called the moisture availability. From the definition of M in (2.65) it is easily seen that M is constrained to vary between 0 and 1. As the canopy resistance goes to zero, M goes to 1. And as the canopy resistance becomes very large, M goes to zero. The canopy resistance represents the resistance the plant canopy must work against to obtain water from the soil.

Unfortunately, there is no real reason to suppose that $q_S(T_g)$ is proportional to $q(z_{0v})$. Perhaps the worst-case scenario to examine is a rain forecast in which the very tall tree canopy, perhaps 70 m above the ground, has a temperature and moisture flux that is quite unrelated to what happens at the ground and to the ground temperature. Typically, models that use moisture availability overestimate Q_E in humid regions (Sato *et al.* 1989).

2.5.1 Moisture availability

If one is interested in using M as a method to help calculate the latent heat flux, then are there any physical variables that can be related to M? Perhaps the soil volumetric water content (Θ) and field capacity (Θ_{fc}) could be related to M. Volumetric water content is defined as the ratio of the cubic meters of water in the soil to the cubic meters of dry soil. Soil field capacity is defined as the maximum volume of water a given unit volume of soil can hold after drainage. This can be determined experimentally by putting soil into a container with a sieve at the bottom, and pouring water into the soil until it is saturated and water is dripping out the bottom of the container. When the water stops dripping, the soil is at its field capacity. Thus, one can relate M to the volumetric water content and the field capacity using the formulas from Lee and Pielke (1992), where

$$M(z) = \frac{1}{4}\left\{1 - \cos\left[\frac{\Theta(z)\pi}{\Theta_{fc}}\right]\right\}^2 \qquad \text{for} \quad \Theta < \Theta_{fc}, \tag{2.66}$$

$$M(z) = 1 \qquad \text{for} \quad \Theta \geq \Theta_{fc}. \tag{2.67}$$

In models that use M, typically the value of M is fixed or varies only slightly during the course of a day. However, since M is defined in terms of r_c, one should be aware that r_c varies during the daytime hours. In fact, r_c is a maximum at sunrise and sunset, and reaches a minimum near solar noon if the vegetation is not stressed (Monteith and Unsworth 1990).

Another approach to determining a value for M is to use an antecedent precipitation index (API). Chang and Wetzel (1991) show an easy approach that uses daily values of API, calculated over a several month period, to specify a value for M. They define

$$API_i = k_{API}\, API_{i-1} + P_i, \tag{2.68}$$

where k_{API} is a decay coefficient ($\sim$0.92 is typical) for a given soil layer and P_i is the precipitation that fell on day i. The precipitation total for a single day is not allowed to exceed a selected maximum value, such that if $P_i > P_m$ then $P_i = P_m$. In Chang and Wetzel (1991), P_m is set to 4 cm. If this formula is used iteratively for several months, the final value should be independent of the initial value of API selected to start the calculations. The best hope for this technique is that the volumetric water content is related to the API value, and from there a soils database can be used to get the field capacity of the soil and thus get an approximation for M.

For historical significance, the bucket approach (Manabe 1969) also was used to define M in many models dating from the 1960s. The bucket approach assumes that a bucket exists at each model grid point. Rain falling into this bucket increases the depth of the water within the bucket. Water is removed from the bucket owing to the amount of latent heat released into the atmosphere. The bucket has a maximum depth, typically assumed to be 15 cm, and any amount of water exceeding this depth runs out the top of the bucket. The value of M is then defined as the height of the water in the bucket divided by the total depth of the bucket. This approach was used in the nested grid model (NGM) and many earlier global circulation models.

2.5.2 *Penman–Monteith approach*

Is there any other way to determine the latent heat flux, since the original definition as shown by (2.64) includes terms that are not really physical? Assume that there is a need to calculate the latent heat flux using conventional surface data. The Penman–Monteith approach is one way to estimate the latent heat flux using surface data (Penman 1948; Monteith 1965) and is derived as follows. We know that, through simple manipulation,

$$\begin{aligned} e_s(T_g) - e_a &= e_s(T_g) - e_a + e_s(T_a) - e_s(T_a) \\ &= e_s(T_g) - e_s(T_a) + [e_s(T_a) - e_a], \end{aligned} \tag{2.69}$$

where e is the vapor pressure, $e_s(T)$ is the saturated vapor pressure at temperature T, T_g is the ground temperature, T_a is the air temperature at 2 m, and e_a is the vapor pressure at 2 m. We also know that we can rewrite

$$\begin{aligned} e_s(T_g) - e_s(T_a) &= \frac{[e_s(T_g) - e_s(T_a)](T_g - T_a)}{T_g - T_a} = \frac{\partial \bar{e}_s(T)}{\partial T}(T_g - T_a), \\ &= \bar{\Delta}(T_g - T_a), \end{aligned} \tag{2.70}$$

where $\bar{\Delta}$ is the change of saturation vapor pressure with respect to temperature and can be approximated by a constant. Combining the results from (2.70) into (2.69), one obtains

$$e_s(T_g) - e_a = \bar{\Delta}(T_g - T_a) + e_s(T_a) - e_a. \tag{2.71}$$

Now, the latent heat flux can be written as

$$Q_E \cong M\frac{e_s(T_g) - e_a}{\gamma R_H}, \tag{2.72}$$

where

$$R_H = \frac{r_H}{\rho c_p}, \tag{2.73}$$

assuming that $r_H = r_V$. Therefore, using (2.71) one can define the latent heat flux as

$$Q_E = \frac{\left[\bar{\Delta}(T_g - T_a) + e_s(T_a) - e_a\right]M}{\gamma R_H}. \tag{2.74}$$

This derivation can be taken a step further by noting that

$$Q_H = \frac{T_g - T_a}{R_H} \quad \Rightarrow \quad T_g - T_a = Q_H R_H, \tag{2.75}$$

which leads to

$$Q_E = M\left[\frac{\bar{\Delta} Q_H}{\gamma}\left(\frac{R_H}{R_H}\right) + \frac{e_s(T_a) - e_a}{\gamma R_H}\right]. \tag{2.76}$$

If it is further assumed that the ground temperature does not change over time, as is true under highly vegetated canopies where this equation is designed to work, then

$$Q_E \cong M\left[\frac{\bar{\Delta}}{\gamma}(R_{NET} - Q_G - Q_E) + \frac{e_s(T_a) - e_a}{\gamma R_H}\right], \tag{2.77}$$

where R_{NET} is the total net radiation from both short and longwave components of the radiation budget. Combining like terms, this equation is simplified a bit further to develop the expression

$$Q_E = \frac{M\left\{[e_s(T_a) - e_a]/R_H + (R_{NET} - Q_G)\bar{\Delta}\right\}}{\gamma + \bar{\Delta}M}, \tag{2.78}$$

which is often called the Penman–Monteith equation. The first term of (2.78) can be viewed as representing the drying power of the air, since it is proportional to the surface layer vapor pressure deficit. The second term of (2.78) can be viewed as the drying power of the sun, since it is dominated by the incoming solar radiation on most days. Potential evapotranspiration is often defined using (2.78) when $M = 1$.

The Penman–Monteith equation circumvents the problem associated with using the saturation vapor pressure at ground temperature to represent the vapor pressure conditions at the Earth's surface, which is particularly severe

over desert regions with very high ground temperature values. However, the Penman–Monteith formulation does not remove the importance of the moisture availability parameter M to the calculation of latent heat flux. And since it was developed for highly vegetated surfaces, it should not be applied over the entire planet without due consideration.

2.5.3 *Priestley–Taylor approach*

Another approach to calculating the latent heat flux from surface observations is the Priestley Taylor equation (Priestley and Taylor 1972). They assume that the latent heat flux is proportional to the drying power of the sun, yielding

$$Q_E = \frac{\alpha(R_{NET} - Q_G)\bar{\Delta}}{\gamma + \bar{\Delta}}. \tag{2.79}$$

This is the same as neglecting the first term in the Penman–Monteith formulation (2.78), or assuming that the atmosphere near the ground surface is saturated. Values of α less than 1 indicate that the soil is dry (0.4 being the driest), while values of α greater than 1 indicate that the soil is reasonably well watered. Davies and Allen (1973) relate the soil volumetric water content to α, such that

$$\alpha = a\left(1 - e^{-b\Theta/\Theta_{fc}}\right), \tag{2.80}$$

where $a = 1.28$ and $b = 10.563$. Thus, $\alpha = 1.28$ for saturated soil conditions as expected, but the value of α can decrease to near zero as Θ/Θ_{fc} decreases below 0.2. Williams *et al.* (1978) and Barton (1979) use the same approach, but find different values for a and b, suggesting that the relationship between α and Θ/Θ_{fc} is not very general. This approach is most appropriate for use over vegetation with shallow roots, or bare soil, although it is not the best choice in truly desert regions. Stull (1988) and Brutsaert (1982) further indicate that the Priestley–Taylor equation can yield incorrect flux values when advection occurs.

2.6 Ground heat flux

The final term in the surface energy budget is the ground heat flux. When averaged over a full 24 h cycle, this term often averages to near zero. This observation led many pioneers using general circulation models to set this term to zero. Another alternative that was used in early studies that forecast the

diurnal cycle was to relate the ground heat flux to the total net radiation. Observations indicate that Q_G is typically between 5% and 15% of the net radiation during the daytime, although this fraction increases to approximately 50% at night. Others tried relating Q_G to the sensible heat flux by defining $Q_G = 0.3\ Q_H$. Deardorff (1978) presents a good summary of these early methods of neglecting or defining Q_G. However, these approximations did not last very long and soon multi-level soil modules were in use in all numerical weather prediction models.

Multi-level soil models include an equation for the ground surface, or skin, temperature plus several specific soil levels below the ground surface. Since the heat transport process is conduction, the amount of heat transferred is proportional to the vertical temperature gradient. Therefore,

$$Q_G = -k_g \frac{\partial T}{\partial z}, \tag{2.81}$$

where k_g is the thermal molecular conductivity, it is assumed that the ground heat flux $Q_G = Q_g$ at the ground surface ($z = 0$), and z increases in the downward direction. Assuming no other sources or sinks of heat, the second law of thermodynamics yields

$$\frac{\partial T}{\partial t} = -\frac{1}{c_g}\frac{\partial Q_g}{\partial z}, \tag{2.82}$$

where c_g is the soil heat capacity and is equal to the soil density multiplied by the soil specific heat ($c_g = \rho_{soil} \cdot c_{soil}$). Assuming that the thermal conductivity is independent of soil depth, then these two equations can be combined to yield the classic heat conduction equation for the ground heat flux,

$$\frac{\partial T}{\partial t} = -\nu_g \frac{\partial^2 T}{\partial z^2}, \tag{2.83}$$

where ν_g is the soil thermal diffusivity ($\nu_g = k_g/c_g$ and varies from 1×10^{-6} to $1 \times 10^{-7}\ m^2\ s^{-1}$). Therefore, one can set up equations for calculating the heat transfer into the ground using selected vertical levels below ground for computation, and given an initial soil temperature profile (Deardorff 1978).

A slightly different approach to predicting the ground heat flux is to simplify the soil model to just two vertical slabs (Bhumralkar 1975; Blackadar 1976). The first slab is in contact with the ground surface and typically represents a soil depth of a few cm. The second slab is considered to be a reservoir and has a constant temperature. Thus, the upper slab responds to both changes in the surface energy balance and conduction from the lower reservoir below.

If the depth of the upper slab is d_s, then a soil heat capacity per unit area can be calculated for the upper slab as $c_G = c_g \cdot d_s$. The equation for the temperature of the slab is then

$$c_G \frac{\partial T_g}{\partial t} = R_{NET} - Q_H - Q_E - \kappa(T_g - T_r), \tag{2.84}$$

where T_r is the reservoir temperature and κ is a soil conductivity. Results indicate that the simulations using this approach are sensitive to the depth of the upper soil layer, with shallower soil layers yielding larger responses, as one would expect. Applications of this approach to handling soil temperatures are found in the land surface parameterizations of Noilhan and Planton (1989) and Mahfouf (1991).

When the thermal conductivity varies with depth, as one might expect when soil moisture is considered, then (2.82) is used (Pan and Mahrt 1987; Viterbo and Beljaars 1995) and the soil heat capacity and thermal conductivity are allowed to vary with soil moisture. The basic equation for the ground heat flux is then

$$c_g \frac{\partial T}{\partial t} = \frac{\partial}{\partial z}\left(k_g \frac{\partial T}{\partial z}\right). \tag{2.85}$$

The heat capacity of the soil is defined as a function of soil volumetric water content, such that

$$c_g = (1 - \Theta_S)c_{soil} + \Theta c_{water}, \tag{2.86}$$

where Θ_S is the soil porosity (the maximum amount of water the soil can hold), c_{soil} is $1.26 \times 10^6\,\mathrm{W\,m^{-3}\,K^{-1}}$ and c_{water} is $4.2 \times 10^6\,\mathrm{W\,m^{-3}\,K^{-1}}$. Values of soil porosity vary between 0.3 and 0.6 depending upon the soil type. Since the heat capacity for water is over three times the value for soil, it is clear that the volumetric water content of the soil has a large role in determining the total heat capacity. Chen and Dudhia (2001) further include a third term to represent the effect of air space within the soil on the heat capacity, although this term is small.

Similarly, the thermal conductivity also is strongly dependent upon the soil volumetric water content. Many models appear to use the formulas suggested by Al Nakshabandi and Kohnke (1965), such that

$$k_g(\Theta) = \begin{cases} 420\exp(-P_f + 2.7), & P_f \leq 5.1, \\ 0.1722, & P_f > 5.1, \end{cases} \tag{2.87}$$

where

$$P_f = \log_{10}\left[\psi_s\left(\frac{\Theta}{\Theta_s}\right)^{-b}\right] \tag{2.88}$$

has units of cm and the values of ψ_s, Θ_s, and b are functions of the soil type and are discussed more fully in the next chapter and in Clapp and Hornberger (1978) and McCumber and Pielke (1981). Mahrt and Pan (1984) emphasize that the values of soil thermal conductivity can vary over orders of magnitude with depth or over time, strongly indicating the need to include the effects of soil moisture in the parameterization.

More recent results that compare the sensitivity of sensible and latent heat fluxes to the soil thermal conductivity suggest that (2.87) and (2.88) may not be appropriate for the entire range of volumetric water content (Peters-Lidard *et al.* 1998). An alternative method developed by Johansen (1975) is proposed and agrees better with observations. However, this method requires knowledge of the quartz content and soil particle size, which are not often known. Thankfully, the quartz content can be related to the sand content of the soils, and the soil particle size appears to have a negligible effect on the results. While the details are presented in Peters-Lidard *et al.* (1998), the general idea is that the soil thermal conductivity is a factor of both the dry (κ_{dry}) and saturated (κ_{sat}) thermal conductivities, such that

$$k_g = K_e(\kappa_{sat} - \kappa_{dry}) + \kappa_{dry}, \tag{2.89}$$

where K_e is the Kersten number and weights the dry and saturated conductivities. The dry thermal conductivity is calculated using

$$\kappa_{dry} = \frac{0.135(1-n)2700 + 64.7}{2700 - 0.947(1-n)2700}, \tag{2.90}$$

where n is the value of soil porosity. The expression $2700(1-n)$ represents the dry soil density in $\mathrm{kg\,m^{-3}}$, where the soil unit weight is $2700\,\mathrm{kg\,m^{-3}}$.

The saturated thermal conductivity of the soil is calculated using

$$\kappa_{sat} = \kappa_s^{1-n}\kappa_i^{n-x_u}\kappa_w^{x_w}, \tag{2.91}$$

where x_u is the unfrozen volume fraction (0 to 1), the ice thermal conductivity $\kappa_i = 2.2\,\mathrm{W\,m^{-1}\,K^{-1}}$, the water thermal conductivity $\kappa_w = 0.57\,\mathrm{W\,m^{-1}\,K^{-1}}$, and the solid's thermal conductivity is determined from

$$\kappa_s = \kappa_q^q \kappa_o^{1-q}. \tag{2.92}$$

Here q is the quartz content (0 to 1), $\kappa_q = 7.7\,\mathrm{W\,m^{-1}\,K^{-1}}$ is the thermal conductivity of quartz, κ_o is the thermal conductivity of other minerals, and is assumed to be $2.0\,\mathrm{W\,m^{-1}\,K^{-1}}$ for $q > 0.2$ and $3.0\,\mathrm{W\,m^{-1}\,K^{-1}}$ otherwise.

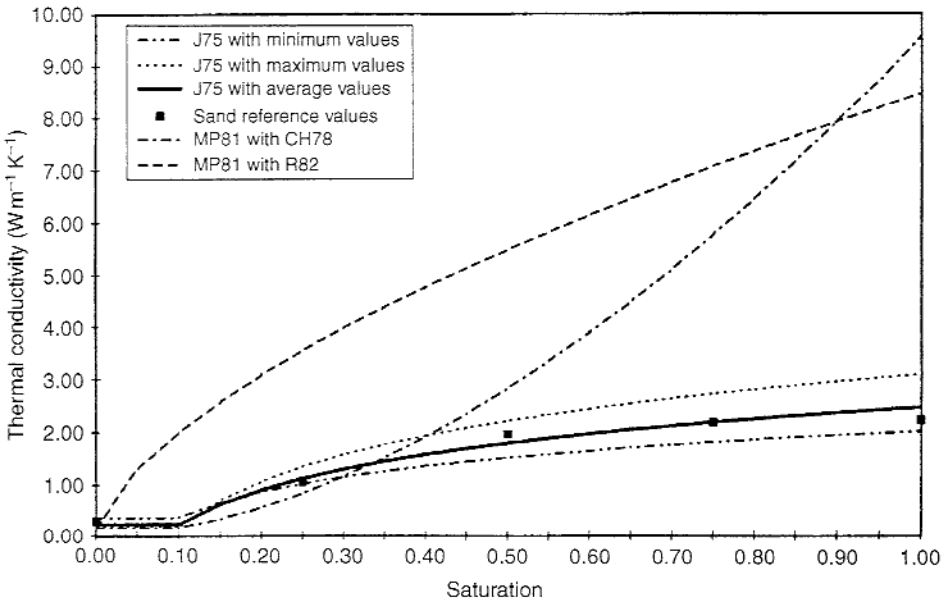

Figure 2.21. Thermal conductivity versus saturation fraction for sand. J75 is the Johansen method, MP81 is the McCumber and Pielke (1981) application of the Al Nakshabandi and Kohnke method, and reference values are indicated by solid squares. CH78 indicates use of the Clapp and Hornberger (1978) soil water retention functions, and R82 indicates use of the Rawls *et al.* (1982) soil water retention functions. From Peters-Lidard *et al.* (1998).

The Kersten number is a function only of the degree of soil saturation S_r. Peters-Lidard *et al.* (1998) provide expressions for the Kersten number for both coarse and fine soils, but consider only fine soils in their analyses and suggest that the differences in predicted values are small. For fine soils, the Kersten number is defined as

$$K_e = \log S_r + 1.0, \tag{2.93}$$

while for frozen soils $K_e = S_r$. Table 2 in Peters-Lidard *et al.* (1998) provides the values of quartz content for the standard 12 United States Department of Agriculture (USDA) soil textures.

A comparison of the thermal conductivities from several approaches indicates that the Johansen (1975) approach appears to compare best with the reference values (Fig. 2.21), whereas the Al Nakshabandi and Kohnke (1965) values are too large when a cap value is not used. Even when the thermal conductivity is capped, the curve from Johansen (1975) appears to fit the reference values better.

Multi-level soil models, with soil heat capacity and thermal conductivity dependent upon the soil volumetric water content, represent one approach to accounting for the detail needed to accurately account for soil processes in land surface parameterizations. The main differences between parameterizations typically involve specification of the various parameter values and the number of vertical soil levels. Mahrt and Pan (1984) illustrate the importance of the thickness of the soil layers to the behavior of soil models, while Santanello and Carlson (2001) suggest that thin near-surface soil layers are needed to capture rapid soil drying. Many soil models in use within operational numerical weather prediction models have four or more vertical soil layers.

2.6.1 Frozen soil

When ground surface temperatures are below freezing, then some of the water in the soil freezes. The effects of this phase change need to be included in the heat conduction equation. It is generally assumed that the only phase change that occurs is between liquid water and ice, the soil does not deform due to the soil freezing and thawing, and there is no transport of ice within the soil. A heat balance equation can then be written (Koren *et al.* 1999; Smirnova *et al.* 2000) such that

$$c_g \frac{\partial T}{\partial t} - L_f S_{li} = \frac{\partial}{\partial z}\left(k_g \frac{\partial T}{\partial z}\right), \tag{2.94}$$

where L_f is the latent heat of fusion (3.34×10^5 J kg^{-1} at 0 °C) and S_{li} is the rate of liquid mass transformation into ice. This equation is identical to (2.85) except for the $L_f S_{li}$ term that accounts for the liquid to solid phase change. The rate of liquid mass transformation into ice is defined as

$$S_{li} = -\rho_l \frac{\partial \Theta}{\partial t} = \rho_l \frac{\partial \Theta_i}{\partial t}, \tag{2.95}$$

where Θ_i is the volumetric ice content. This equation indicates that as the soil volumetric water content decreases due to freezing, the value of S_{li} is positive and ice is created. With some modifications, Smirnova *et al.* (2000) show that the heat balance equation can be rewritten as

$$c_a \frac{\partial T}{\partial t} = \frac{\partial}{\partial z}\left(k_g \frac{\partial T}{\partial z}\right), \tag{2.96}$$

where c_a is the apparent heat capacity and is defined as

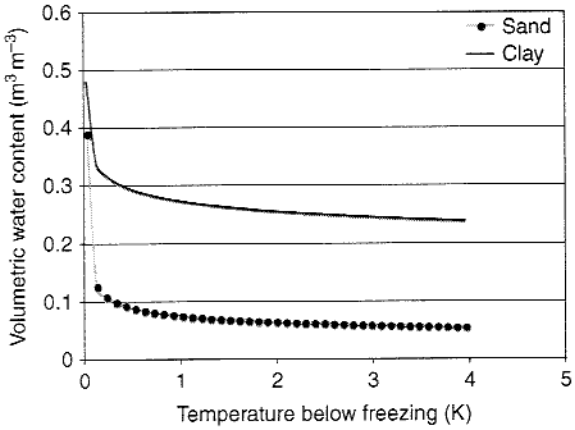

Figure 2.22. Soil-freezing characteristic curves calculated using (2.98) for soil parameters appropriate for sand (gray line) and clay (black line).

$$c_a = c_g + \rho_l L_f \frac{\partial \Theta}{\partial T}. \tag{2.97}$$

The slope of the soil-freezing characteristic curve $\partial\Theta/\partial T$, the relationship between frozen volumetric water content and temperature, is obtained empirically (Cary and Maryland 1972; Flerchinger and Saxton 1989). Smirnova *et al.* (2000) suggest that the slope of the soil-freezing characteristic curve can be represented using

$$\Theta = \Theta_S \left[\frac{L_f (T - 273.15)}{g T \psi_S} \right]^{-1/b}, \tag{2.98}$$

where ψ_S is the soil moisture potential for a saturated soil (units of m), has a value less than zero, and depends upon the soil type, and b and Θ_S also are constants that depend upon soil type (see Chapter 3). The general shape of the soil-freezing characteristic curve is shown in Fig. 2.22 and indicates that most of the liquid water in sandy soils becomes ice when the temperature is only 1 °C below freezing; it takes much colder temperatures for the same amount of water in clay soils to freeze and some fraction of the soil water may never freeze. Other models assume that all the water in the soil freezes when the temperature is below a given threshold value several degrees below freezing.

Once ice is present in the soil, it influences the soil heat capacity. Thus, the definition of the soil heat capacity must be modified to include the effects of ice, yielding

$$c_g = (1 - \Theta_S) c_{soil} + \Theta c_{water} + \Theta_i c_{ice}. \tag{2.99}$$

The presence of ice also modifies the thermal conductivity k_g. Koren *et al.* (1999) use a simple linear adjustment suggested by Kutchment *et al.* (1983) to define

$$k_g(\Theta, \Theta_i) = k_g(\Theta)(1 + \Theta_i), \tag{2.100}$$

whereas Smirnova *et al.* (2000) define the thermal conductivity following Pressman (1994) as

$$k_g(\Theta, \Theta_i) = k_g(\Theta)\left(1 + \frac{\rho_i}{\rho_l}\Theta_i\right), \tag{2.101}$$

where ρ_i is the density of ice. Luo *et al.* (2003) compare the results of frozen soil parameterizations from 21 land surface schemes over Valdai, Russia, and find that the inclusion of soil-water freezing improves the simulations of soil temperature on seasonal and interannual timescales.

Parameterizations that are concerned with frozen soil also typically include some representation of snow cover and its effects on heat transport as well. Both Koren *et al.* (1999) and Smirnova *et al.* (2000) include simple snow models. These models both approximate the effects of snow on heat transport, including the effects of snow accumulation and snow melting from the snow–air interface and from the snow–soil interface. Koren *et al.* (1999) further include an approximation to snow compaction. Neither approach presently includes the refreezing of snow meltwater and the storage of liquid water within the snow. Slater *et al.* (2001) compare the simulations of snow from 21 land surface schemes as part of the Project for the Intercomparison of Land–Surface Parameterization Schemes (PILPS) and find systematic differences between the parameterizations over the 18 years of simulation.

Frozen water within the soil also has a significant influence on the ability of water to infiltrate into the soil, thereby influencing runoff. A discussion of these effects may be found in Chapter 3 where a more complete discussion is conducted on the determination of soil volumetric water content.

2.7 Surface energy budget equation

All the terms in the surface energy budget have now been defined. To conserve energy at the Earth's surface, all gains and losses of energy must balance. Thus, the surface energy budget valid at the Earth–atmosphere boundary can be defined as

$$Q_S - Q_{Lu} + Q_{Ld} = Q_H + Q_E + Q_G, \tag{2.102}$$

where Q_S already includes the effects of albedo as defined by (2.1). While this balance is maintained over time, the individual terms vary in magnitude and the values of Q_H, Q_E, and Q_G can change sign. During the daytime with large Q_S, the signs of Q_H, Q_E, and Q_G typically are positive in (2.102), indicating upward directed surface heat fluxes and a downward directed ground heat flux. Recall that the specification of these fluxes as having positive or negative values during the daytime as energy is transferred from the ground surface to the atmospheric surface layer varies in the literature, so pay attention to the direction of the energy flux to determine what sign convention is used within a given model.

2.8 Representation of terrain

The terrain field developed for a numerical weather prediction model is important for a number of reasons. The terrain height defines the depth of the atmosphere above the ground, influencing the amount of solar radiation that reaches the ground surface. As solar radiation heats the ground surface in regions of complex terrain, atmospheric circulations may develop, such as mountain–valley flow systems. These terrain-induced flows may develop clouds, thereby providing a negative feedback to the solar radiation. Terrain also can act to block or channel atmospheric flows, and can lead to the development of mountain waves and downslope winds. Finally, the terrain field is often used to separate the model grid points that are over land versus those that are over water. Thus, it is very important for numerical weather prediction models to have an accurate terrain height defined at each grid point.

Terrain data are generally obtained from digital elevation models (DEMs) created by government agencies, such as the United States Geological Survey (USGS). Global data are available at approximately 1 km spacing, although data with spacing as small as 30 m are available over some regions. However, a variety of data are used to construct global terrain data sets. In addition to point measurements of terrain height at regular horizontal intervals, the terrain heights in some regions of the globe are interpolated from terrain contour maps produced by a variety of agencies. Thus, the accuracy of the terrain data varies somewhat from location to location. In general, terrain heights at 1 km spacing have an estimated root-mean-square error as small as 9 m over well-sampled regions and as large as 300 m when derived from maps with 1000 m height isolines. It is important to understand the source of the terrain data used in the model so that the uncertainties in terrain height over the forecast area of interest are recognized.

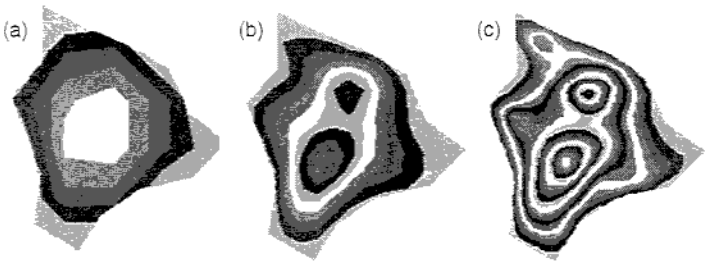

Figure 2.23. Terrain field over the island of Hawaii represented using (a) 30 km, (b) 10 km, and (c) 5 km grid spacing. Terrain heights are shaded every 400 m in all panels. Note the much greater terrain detail as the grid spacing is decreased, as well as the increase in maximum terrain height as indicated by the greater number of alterations in shading. At 30 km, the highest terrain point is 1892 m, whereas at 10 km it is 2974 m and at 5 km it is at 3918 m. The actual peak of Mauna Loa is at 4169 m. Also note the northern displacement of the highest terrain in (a) compared to (b) and (c). In addition, the higher northern peak of Mauna Kea (4205 m) is seen using 5 and 10 km grid spacing, but is not seen at all using 30 km grid spacing. Finally, the Kohala Mountains stretching southeast to northwest along the northern tip of Hawaii are clearly seen using 5 km grid spacing, but are missed even at 10 km grid spacing.

Once the terrain data are available, and the grid spacing for the numerical weather prediction model is defined, interpolations are made from the terrain data to the model grid. Some averaging of the terrain data is often necessary to represent the terrain field in the model appropriately. As the model grid spacing decreases, the terrain field represented in the model becomes more realistic (Fig. 2.23).

However, the subgrid variability of terrain is also important. Results from medium-range forecast models and general circulation models during the 1970s and 1980s for the northern hemisphere cold season indicate that the zonally averaged upper-tropospheric flow was too strong in the midlatitudes (Lilly 1972; Palmer *et al.* 1986). This systematic error influences the predicted values of sea-level pressure, low-level winds, geopotential heights, and the evolution of extratropical cyclones. This error is due to the lack of sufficient drag from rugged mountain ranges, which influences the stationary waves in the atmosphere (Wallace *et al.* 1983). As described by Palmer *et al.* (1986), in stratified flow a drag force can be imposed on the atmosphere via internal gravity waves. These waves have horizontal wavelengths of ~6 km for flow over a hill of width 1 km. Thus, if the model grid spacing is greater than 10 km, there can be a significant underestimation of the drag force exerted by

mountain ranges (Clark and Miller 1991). This systematic wind speed error does not exist during the warm season, when the atmospheric stratification is lower and the surface winds weaker. It also does not exist when the elevated terrain varies smoothly, such as over plateaus, and there is little subgrid variation in terrain height. Parameterizations to account for subgrid orographic drag are discussed in Chapter 10.

2.9 Discussion

One of the key pieces of information that influences the surface fluxes of sensible and latent heat is the wind profile near the surface. As seen throughout this chapter, this log wind profile is paramount in the calculation of resistances. Yet the land surfaces for which this profile has been observed are limited. Many of the observational results are from surface and boundary layer experiments over relatively flat terrain and with uniform vegetation coverage (see Garratt and Hicks 1990; Kaimal and Wyngaard 1990). It is not at all clear that the log wind profile relationship, including corrections and adjustments for non-neutral conditions, is appropriate for regions where vegetation changes are dramatic or terrain changes are rapid. Dyer (1974) clearly shows that changes in surface roughness, as could be created by changes in vegetation type, produce fluxes that do not correspond to the environmental profiles directly above. The inaccuracy that this type of situation produces in the calculated values of resistance is uncertain. While there have been several planetary boundary layer experiments in regions of complex terrain (e.g., Schneider and Lilly 1999), there remains much to be learned. This is especially true since the surface fluxes set the stage for what happens later in the day in terms of convective development.

It also is evident that there are several other uncertainties involving the calculation of surface fluxes, especially the latent heat flux. Some approaches use the ground temperature to obtain a saturation specific humidity, while others are based upon the air temperature instead. Both approaches are valid, but yield very different values for potential evaporation (when $M = 1$) and have different sensitivities, and are likely to have different error characteristics. This highlights the complexities one faces when using a numerical model, and the choices that have to be made in how to parameterize processes that the model cannot resolve explicitly. These types of choices are seen again and again in numerical prediction models.

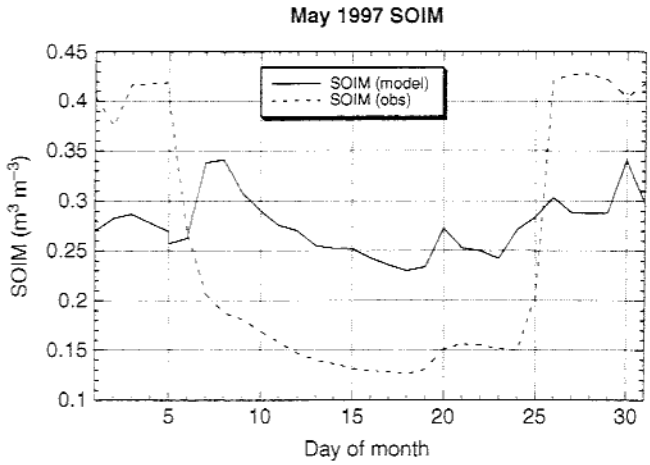

Figure 2.24. Time series comparison of model and observed 5 cm soil volumetric water content (SOIM) at Norman, Oklahoma, during May 1997. Values plotted are daily averages of hourly observations and Eta model data. From Marshall *et al.* (2003).

When thinking about how numerical weather prediction models are initialized, the meteorological community has invested a lot of time, effort, and expense towards better observations of the atmosphere. Satellite, aircraft, and radar data are all now being assimilated into models. But there is precious little information on what is occurring below the ground surface. Measurements of soil temperature and soil moisture are few and far between. Marshall *et al.* (2003) show that the Eta model initial values of soil moisture are very different from observations provided by the Oklahoma Mesonet (Fig. 2.24). Similar results are suggested when comparing the Eta model initial soil temperatures with observations (Godfrey *et al.* 2005). Since soil temperature and moisture play an important role in the calculations of sensible, latent, and ground heat flux, it is not clear why more resources are not directed towards soil measurements. The uncertainty in the soil initial states clearly represents one source of error in numerical weather prediction today.

The discussions in this chapter highlight the ever-increasing need for collaboration across the many sciences that study processes that influence the atmosphere. Whether botany, soil science, oceanography, or chemistry, the need for multidisciplinary communication has never been greater. The atmosphere can no longer be viewed and studied in isolation, and teaching new generations of meteorologists to be aware of and interact with scientists in other disciplines is of enormous importance. The motivation behind this viewpoint becomes even clearer in the following chapters.

2.10 Questions

1. The following mean wind data, sampled at various heights, occur above a vegetated canopy. Find the displacement depth d for this canopy.

Height (m)	Wind speed ($m\,s^{-1}$)
10	7.11
12	8.01
14	8.63
16	9.11
20	9.81
30	10.92
40	11.63

   Typically, if $\ln(z - d)$ is plotted versus wind speed, the line will be concave upward if d is too small and concave downward if d is too large.
2. Given that $T_g = 302$ K, $T_{10\,m} = 294$ K, $Q_H = 300\,W\,m^{-2}$, and $\rho = 1.0\,kg\,m^{-3}$, calculate the resistance to sensible heat flux in the layer from the surface to 10 m above the surface. Assuming $T_{2\,m} = 294.5$ K and $z_0 = 0.01$ m, what is the resistance from the surface to 2 m? Using this knowledge, estimate the resistance to sensible heat flux in the lowest 20 m above the surface and determine the temperature at this level. Is this temperature profile realistic? State any assumptions made and show all work.
3. Calculate the resistances for sensible heat flux assuming that $u(20\,m) = 10\,m\,s^{-1}$ and that there are three different uniform vegetation types: $h = 1.6$ m for one vegetation height, $h = 0.8$ m for another, and $h = 0.1$ m for the third. State any assumptions made. Which resistance is larger? Assuming a 10 K temperature potential, calculate the differences in sensible heat flux from these three resistances. What does this say about the importance of the roughness length in models?
4. Using the same three vegetation types as described in Question 3, calculate the resistances to latent heat flux. Assuming a $0.02\,kg\,kg^{-1}$ specific humidity potential ($\Delta q = q_s(T_g) - q(z)$) and a canopy resistance of $200\,s\,m^{-1}$, what are the latent heat fluxes for the three vegetation heights? Do the changes in the relative values of latent and sensible heat fluxes over the three different vegetation types make sense? What is the value of moisture availability?
5. Draw a typical diurnal cycle for each of the terms (R_{net}, Q_G, Q_E, and Q_H) of the surface energy budget. Then draw an energy flux diagram and show the magnitudes and signs of each term at 1200 local noon and 0400 local morning (before sunrise). Why are these values realistic? Explain.
6. Write a computer program to calculate the change in surface temperature over an entire daytime heating cycle (sunrise to sunset) using the force-restore method. Assume that the calculation is for near Amarillo, Texas on 30 June

1999 (35.2° latitude, −102.0° longitude), and begin the calculations at sunrise and end the calculations at sunset. To actually do this without attaching the surface to a boundary layer model, we have to make some pretty stringent assumptions. Assume the atmospheric transmissivity is constant at 0.8, the solar constant is 1368 W m^{-2}, the thermal capacity of the slab (c_g) is 1.4×10^5 J m^{-2} K^{-1}, the skies are clear, the Bowen ratio is 0.7, the temperature at 40 hPa above the ground surface is equal to 25 °C, the initial temperature of the ground surface (skin temperature) is 23 °C, the reservoir temperature is 25 °C, the precipitable water is 2.5 cm, the emissivity is 0.95, and the albedo is 20%. Run two experiments. First, assume the sensible heat flux is 15% of the net radiation received at the surface, and second assume that the sensible heat flux is 30% of the net radiation received at the surface. Plot the radiation amounts on one graph, show the change in ground (skin) temperature on another, and plot the various surface fluxes (sensible, latent, and ground) on yet another graph. What is the phase relationship between the ground (skin) temperature and the heat flux into the ground? What are the times of sunrise and sunset? What is the maximum value of incoming solar radiation?

Remember that

$$\frac{\partial T_g}{\partial t} = \frac{1}{c_g}\left[Q_S + Q_{Ld} - Q_{Lu} - Q_H - Q_E - \kappa(T_g - T_r)\right],$$

where κ is assumed to be constant at 11 J m^{-2} K^{-1} s^{-1} and T_r is the reservoir temperature (K). It is assumed that the energy loss due to the surface albedo is already included in Q_S.

7. Seguin and Gignoux (1974) made wind speed measurements at a number of heights over two adjacent, yet very different, regions. One region consisted of cypress hedges 7 m in height and separated by short grass roughly 10 cm tall. The other region consisted of grass only with a height of roughly 40 cm (see Fig. 2.25). Both regions were large and separated by sufficient distance to allow them to be considered independent regions. The wind speeds at the top of the surface layer at 50 m

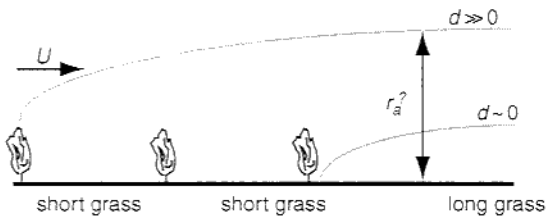

Figure 2.25. Two regions: one of regularly spaced hedges with short grass in between the hedges, and the other of longer grass. Note that the internal boundary layers formed within these two regions are different, and have log wind profiles with different displacement depths (d), and that the internal boundary layer from the hedge region is advected over the internal boundary layer of the grass-only region. The opposite would occur if the wind direction shifts 180°. After Seguin and Gignoux (1974).

above ground level (over which the flux profile laws apply) were virtually identical above both the cypress hedges and the 40 cm grass regions. However, the profiles down to the ground were different. The log wind profile in the grass-only region simply responded to a surface of grass 40 cm high. The log wind profile in the hedge region first responded to a vegetation canopy at the height of the cypress hedges (7 m), while the log wind profile below the hedge top responded to the short grass (10 cm). The height of the hedge top is where they observed this change in the log wind profile behavior in the region with hedges.

(a) Calculate and show graphically the wind speed profiles in the two regions and the difference in wind speed at hedge top level and at 2 m between the hedge and grass-only regions for a wind speed of $10\,\mathrm{m\,s^{-1}}$ at 50 m. Assume neutral static stability. (Note that the two wind regimes in the hedge region must be meshed. The upper regime has a different roughness from the lower.) Calculate the three relevant friction velocities for the problem. Helpful hint: $z_0 \approx h/8$, where h is the average height of the grass or hedge. Comment on the differences in wind speed between the two regions.

(b) Calculate the values of resistance to sensible heat flux from the surface to 50 m for the two regions. Assuming a potential difference of 10 K, what are the values of heat flux over these two regions? If the grass-only region, as depicted at the far right of Fig. 2.25, has the cypress hedge internal boundary layer above it, how might one estimate the change in resistance to heat flux above the grass-only region? Using this estimation technique, how large a difference does this make to the value of resistance?

(This question is based upon course notes from a bioclimatology class taught by Dr. Toby Carlson at The Pennsylvania State University in the late 1980s. I thought the question was excellent at the time and still think it illustrates many important points.)

8. At a given surface observing site, the roughness length is 0.1 m, and at a particular time during the daytime the friction velocity $u_* = 0.85$. The site has two heights at which temperature is observed: 10 and 2 m. The 10 m temperature is 295.4 K and the 2 m temperature is 298.0 K. Determine the ground temperature and the surface sensible heat flux.